Insights into Dopant Mediated Tuning of Silica-Supported Mo Metal Centers for Enhanced Olefin Metathesis

Anoop Uchagawkar[1,2], Anand Ramanathan[1], Hongda Zhu[1,2], Linxiao Chen[3], Yongfeng Hu[4], Justin Douglas[5], Marco Mais[6], Takeshi Kobayashi[6], and Bala Subramaniam[1,2*]

[1]*Center for Environmentally Beneficial Catalysis, The University of Kansas, Lawrence, KS 66047, aited States.*

[2]*Department of Chemical and Petroleum Engineering, The University of Kansas, Lawrence, KS 66045, United States.*

[3]*Department of Chemical, Biomolecular, and Corrosion Engineering, The University of Akron, Akron, OH 44304, United States.*

[4]*Canadian Light Source, University of Saskatchewan, Saskatoon, SK, S7N 2V3, Canada.*

[5]*NMR Core Laboratory, The University of Kansas, Lawrence, KS 66045, United States.*

[6]*U.S. Department of Energy, Ames National Laboratory, Ames, Iowa 50011, United States.*

*Email: bsubramaniam@ku.edu

ABSTRACT

We show that the electronic environment around active Mo centers supported on mesoporous silicates can be tuned by the addition of transition metals creating highly dispersed bimetallic catalysts that display enhanced activity for ethylene + 2-butene metathesis to propylene. The bimetallic catalysts are prepared by incorporating electrophilic Lewis acid metals (M) such as Nb, Ta, Zr or Hf as dopant promoters into mesoporous KIT-6 supports using a one-pot sol-gel technique followed by impregnation of the Mo species. All the prepared bimetallic Mo/M-KIT-6 catalysts display activity with (Mo/Nb-KIT-6) catalysts exhibiting maximum propylene formation rates (54.2 ± 0.5 mmol $(mol_{Mo}\ s)^{-1}$) compared to monometallic Mo/KIT-6 catalyst (28.7 ± 1.1 mmol $(mol_{Mo}\ s)^{-1}$) with an identical Mo loading suggesting that Mo is better utilized in the presence of dopant promoter. Comprehensive catalyst characterization results (deploying HAADF-STEM, DR UV-Vis, XPS, and XAS) qualitatively show an increased population of the four-coordinated Mo-sites in the promoted Mo catalysts, while Raman reveals the presence of Mo dioxo species (O=Mo=O) on both the monometallic and promoted bimetallic catalysts. These results suggest that the addition of transition metals alters Mo coordination yielding isolated bimetallic precursors $[(O=)_2Mo(\text{-}O\text{-}M)(\text{-}O\text{-}Si)]$ in addition to the conventional $((O=)_2Mo(\text{-}O\text{-}Si)_2)$ species. Further, the intrinsic propylene formation rates on the bimetallic formulations follow a linear correlation with the Lewis acid strengths exhibited by the Mo dioxo species (O=Mo=O) revealing that catalyst activity can be enhanced by incorporating a second metal with increasing electrophilic character. Complementary ^{15}N pyridine solid-state NMR spectra display different chemical shifts associated with the metal centers suggesting that four-coordinated dioxo MoO_x species with varying geometric and electronic configurations exist, depending on the added metal. A similar linear correlation was also observed between the average chemical shifts of the adsorbed ^{15}N pyridine and the Lewis acid strengths ($\Delta H_{ads,pyridine}$), providing informative descriptors regarding the molecular origins of the electronic effects influencing olefin metathesis on Mo-based catalysts. Our results demonstrate that simple synthetic methods can be harnessed in general for tuning the electronic environment around metal centers in heterogeneous catalysts for enhancing activity and selectivity.

KEYWORDS: olefin metathesis, bimetallic molybdenum catalysts, metal dopants, niobium, mesoporous silicate supports

1 INTRODUCTION

Propylene is an important precursor for making commodity chemicals such as polypropylene, and propylene glycol. Declining refining capacity in the U.S., caused mainly by the energy transition in the transportation sector, will decrease naphtha output resulting in decreased ethane and propane supply as chemical feedstocks. Ethane sourced from shale gas can bridge the ethane gap in the U.S. However, the propane gap poses a substantial challenge that requires propylene production from other sources.[1, 2] Various on-demand propylene technologies are therefore receiving attention.[3-5] In one scenario, ethylene sourced from either shale gas or biogenic sources may be converted to propylene via cross-metathesis with 2-butene (derived from the dimer of ethylene).[6] Among transition metals, supported Mo and W are the commonly used industrial catalysts for upgrading light olefins via metathesis.[7, 8] While W-based catalysts are active at >400 °C, Mo-based catalysts have been reported to be active at lower temperatures (25-200 °C). However, both catalysts experience selectivity loss due to competing isomerization and cracking side reactions.[8-13] Further, supported Mo catalysts possess ill-defined surface structures that contain only a very small fraction of active sites (ca. 2-5%), limiting the overall catalytic performance.[8, 11] This also renders identifying and understanding the nature of the active sites a challenging task.

The choice of supports significantly influences the catalytic activity of the supported metal oxides (W, Mo, or Re). For example, Mo-incorporated mesoporous silicates such as Mo-EISA[14] and Mo-TUD-1[15] demonstrate 3-4 fold higher metathesis activity compared to Mo/SiO_2. The higher activity was attributed to increased population of the isolated dioxo species (O=Mo=O) in the precatalysts. Recently, Skoda et al. reported that the porous molybdenum silicate nanospheres catalyst shows twofold greater propylene metathesis activity compared to supported MoO_x

prepared by incipient wetness technique,[16] The higher activity is attributed to increased dispersion of MoO_x species. Further, MoO_x-based metathesis catalysts supported on SiO_2-Al_2O_3 mixed oxide materials perform better than those supported on Al_2O_3 or SiO_2.[10, 12, 17, 18] Hahn et al. reported that the SiO_2-Al_2O_3 supported MoO_x catalyst shows high initial metathesis activity at relatively low temperature (~150 °C). This is attributed to an increased population of Brønsted acid sites that favor the *in situ* formation of active Mo-carbene species (Mo=CHR).[12] It has also been reported that on supported MoO_x catalysts, the Brønsted acid sites favor isomerization and oligomerization reactions leading to the formation of heavier hydrocarbons that deactivate the catalysts.[8, 9, 15] Several pretreatment procedures have been reported to increase the metathesis activity of Mo/SiO_2 catalysts. Photoreduction in CO followed by chemisorption in cyclopropane,[19] activation with organosilicon reductants[20] and co-feeding electron-rich promoters[21, 22] are reported to create more active Mo=CHR species. High-temperature (~550-650 °C) pretreatment in methane, propylene or pure H_2 has also been reported to facilitate metal carbene formation (Mo=CHR).[13, 23, 24]

Another approach to enhance catalytic activity and stability is to introduce metal promoters. While bimetallic catalysts have been investigated in a wide variety of reactions,[25-27] they are less explored for olefin metathesis. Recently, the Subramaniam group showed that doping W-based catalysts with small amounts of promoters, such as Nb, significantly enhanced the metathesis activity.[28] This was attributed to the formation of new W-based dioxo species ($(O=)_2W(-O-Nb)(-O-Si)$) on the precatalysts, where the promoter metal in the support framework of silica tunes the electronic environment surrounding the active W center, akin to ligand effects in organometallic chemistry. Density Functional Theory (DFT) calculations showed a linear correlation of the variation in the predicted bond angle (O=W=O) with the observed propylene yield. Zhang et al. reported that anchoring MoO_x species on the most acidic hydroxyl group of Ta-modified Al_2O_3

supports results in a greater number of active sites, facilitating *in situ* formation of Mo=CHR species.[29] Ostroshchenko and coworkers reported similar activity enhancements by introducing inorganic promoters in the silica supports or using modified mixed supports.[30, 31] To better understand the reported promotional effects in bimetallic metathesis catalysts, a detailed understanding of the structure of the active site precursors (i.e., precatalysts) including the role of metals and their oxidation states in promoting catalyst activity is required.

In this work, we seek to explain fundamental electronic and structural effects of Mo-sites in dopant-mediated bimetallic precatalysts by combining intrinsic rate measurements with advanced spectroscopic tools to gain insights into the structure-activity correlations. Toward this end, we investigated the metathesis activity of Mo-based bimetallic catalysts with different promoter metals such as M = Nb, Ta, Zr, or Hf synthesized using a one-pot sol-gel technique. These transition metals were chosen based on the differences in electronegativity and Lewis acid strength among them. We demonstrate that, as reported previously with promoted W/KIT-6 catalysts,[28] enhancements in metathesis activity are also observed in Mo-based bimetallic catalysts when doped with metals such as Nb, Ta, Zr, or Hf. Comprehensive catalyst characterization results deploying a suite of spectroscopic techniques (including HAADF-STEM, DR UV-Vis, XPS, and XANES) show an increased abundance of the isolated four-coordinated Mo-sites, while Raman reveals the presence of structurally similar Mo dioxo species (O=Mo=O) on the monometallic and bimetallic precatalysts. Additionally, we demonstrate that the enhanced propylene formation rates on bimetallic Mo-based mesoporous silicates correlate with increasing strength of the Lewis acid sites in these catalysts as inferred from the adsorption enthalpies ($\Delta H_{ads,\,py}$) of pyridine and the ^{15}N average chemical shifts (δ_{avg}) of the pyridine coordinated to Lewis acid metal centers from ssNMR spectroscopy. Complementary ^{15}N NMR spectra for the bimetallic catalysts show distinct

spectroscopic shifts in the Lewis acid range, suggesting that the electronic environments around the Mo-sites of the precatalysts are tuned by the addition of the second metal. These findings reveal general design principles and techniques that can be harnessed to favorably tune the activity of isolated sites on supported catalysts.

2 EXPERIMENTAL

2.1 Materials

Triblock copolymer Pluronic P123 (EO_{20}-$PO_{70}EO_{20}$, average molecular weight MW=5800), tetraethyl orthosilicate (TEOS, 98%), and zirconyl chloride octahydrate ($ZrOCl_2 \cdot 8H_2O$, 98% reagent grade) were purchased from Sigma Aldrich. Hydrochloric acid (certified ACS plus grade), 1-butanol (>99.5%), water (HPLC grade distilled water, 0.2 micron filtered, niobium(V) chloride ($NbCl_5$, 99.95%), tantalum(V) chloride ($TaCl_5$, anhydrous 95.0+%, TCI America), hafnium (IV) bromide ($HfBr_4$, anhydrous, 98%, Stream Chemicals), and sodium sulfate anhydrous (Na_2SO_4, ≥99%) were purchased from Fisher Scientific. Ammonium heptamolybdate tetrahydrate (≥99%, $(NH_4)_6Mo_7O_{24}\cdot 4H_2O$) was purchased from Acros Organics. Pyridine (≥99.8%) for in situ pyridine DRIFTS measurements was purchased from EMD millipore. For ssNMR experiments, deuterated pyridine-d_5 (≥99.5 atom% D) and pyridine-^{15}N (98 atom% ^{15}N) were purchased from Sigma Aldrich. (Ethylene (CP grade, ≥99.5%), 2-butene (≥95.5 wt.%, 39% cis-2-butene and 61% trans-2-butene), 1-butene (CP grade, ≥99.5%), 10% O_2/N_2 (HP, 99.9%), nitrogen (N_2) (UHP, 99.99%), argon (Ar) (UHP, 99.99%), 10% H_2/Ar hydrogen (UHP, 99.99%), helium (He) (UHP, 99.99%), and air (UHP, 99.99%) were all purchased from Matheson Tri-Gas Inc. All the chemicals were used as received. The ethylene and 2-butene feed gases were purified over anhydrous sodium sulfate (Fischer scientific) traps to remove moisture traces that can inhibit the metathesis activity.

All the other gases were purified over a molecular sieve (3 Å) moisture trap prior to entering the reactor.

2.2 Catalyst synthesis

We synthesized a series of monometallic Mo_x/KIT-6 and the bimetallic Mo_x/M_y-KIT-6 (Mo_x/M_y) catalysts with various Mo and dopant metal (M = Nb, Ta, Zr, or Hf) loadings ('x' represents Mo loading and 'y' represents dopant promoter metal loading in wt%). The transition dopant promoters were chosen based on the differences in electronegativity and Lewis acid strengths. We employed a one-pot sol-gel technique[28] to synthesize highly dispersed and isolated M-O-Si framework (My-KIT-6), followed by simple impregnation of Mo on My-KIT-6 materials using ammonium heptamolybdate as Mo precursor. In a typical synthesis, 4 g of Pluronic P123 copolymer was dissolved in 140 ml water and 6.1 g of hydrochloric acid (HCl, 35 wt%) under stirring at a constant temperature of 35.0 ± 2 °C for 24 h. Later, 4 g of 1-butanol were added to the solution and stirred for another 4 h. At this time, 8.7 g of tetraethylorthosilicate (TEOS) and appropriate amounts of metal (M) precursor (to yield 0.5, 1, 1.5, and 2.5 wt% metal in the synthesis gel) were added simultaneously to the solution with vigorous stirring at the same temperature for another 24 h. The resulting sol-gel mixture was transferred to a Teflon-lined autoclave for hydrothermal treatment at 100 °C for 24 h. After this treatment, the reactor was cooled to room temperature, and the contents were vacuum filtered without any further washing. The wet solid layer was dried in an oven at 100 °C for 12 h. Finally, the organic contents (template) in the dried solids were removed by calcination in flowing air (100 std cm^3/min or sccm) at 550 °C (heating rate of 1 °C/min) for 10 h. The synthesized samples are designated as M_y-KIT-6 where M represents Nb, Ta, Zr, or Hf, and y represents the wt% loadings (y = 0.5, 1, 1.5, and 2.5 wt%) of the respective M in the synthesis gel.

The monometallic Mo_x/KIT-6 and the bimetallic Mo_x/M_y-KIT-6 (Mo_x/M_y) catalysts with various Mo loadings (x = 2, 3, 5, and 7 wt%) were synthesized using a previously reported wet impregnation technique.[15] The impregnated slurry solution is dried in a rotavap evaporator at ca. 45 °C and later in an oven at 100 °C for 12 h. Finally, the dried solids are ground gently and calcined in flowing air (100 sccm) at 550 °C (heating rate of 1 °C/min) for 5 h. The elemental compositions in all the catalyst samples were determined using X-ray Fluorescence (XRF) technique.

2.3 Catalyst textural characterization

Characterizations were performed on the freshly calcined and spent catalyst samples. The physicochemical properties of the catalyst samples were examined using XRD, XRF, BET and HAADF-STEM techniques (see Supporting Information Secs. SB1.1-SB1.3, Figures S1-S3). Wide-angle x-ray diffraction (XRD) patterns were collected using a Malvern Panalytical Empyrean instrument with Cu Kα radiation (45kV, 40mA, λ = 0.154 nm). The XRD data were recorded between 2θ values of 5 – 80º and a total scan time of 20 min. The elemental compositions were measured using XRF (Malvern Panalytical Zetium instrument). The total surface area (meso and micro-pore areas), pore volume and pore size distribution were measured using nitrogen adsorption-desorption experiments at liquid N_2 (77 K) using the Brunauer-Emmett-Teller (BET) and Barrett-Joyner-Halenda (BJH) theories.

3 RESULTS AND DISCUSSION

3.1 Physiochemical characterization

All the catalyst samples displayed type IV isotherm and H1 hysteresis loop indicative of ordered mesoporous silicates with high uniformity in pore size (Figure S2, Sec SB1.2)[32], also

evident in HR-TEM and the STEM-HAADF images (Figure S3 (a, b), Sec SB1.3), The textural properties are summarized in Table S1.

For the $Mo_2/Nb_{1.5}$-KIT-6 catalyst, the HAADF-STEM image and the elemental mapping show higher dispersion of the MoO_x species on the catalyst surface along with highly dispersed NbO_x species (elemental mapping) yielding subnanometer Mo particles ($dp = 0.7 \pm 0.2$ nm). In contrast, the Mo_2/KIT-6 catalyst revealed a slightly broader particle size distribution of Mo nanoclusters (dp ~1.1 ± 0.4 nm). This suggests enhanced Mo dispersion in the case of Nb-incorporated bimetallic catalyst.

XPS measurements were performed to probe the oxidation states and the distribution of the surface MoO_x species on the fresh Mo_2/KIT-6 and the bimetallic $Mo_2/M_{1.5}$-KIT-6 catalysts. All the bimetallic $Mo_2/M_{1.5}$-KIT-6 catalysts show a dominant presence of Mo^{VI} species (Figure S4 (a-e)). The presence of reduced MoO_x species (Mo^{V} and Mo^{IV}) is evident in all the catalyst samples, being the highest in the unpromoted Mo_2/KIT-6 sample (68%), followed by $Mo_2/Ta_{1.5}$ (~52%), and $Mo_2/Hf_{1.5} \approx Mo_2/Zr_{1.5}$ (41%) (Figure S4g). The Mo 3d doublet ($3d_{5/2}$ and $3d_{3/2}$) spectrum is especially well resolved in $Mo_2/Nb_{1.5}$-KIT-6 catalyst (Figure S4b) and exclusively contained Mo^{VI} species, consistent with the results from DR UV-Vis and TEM analyses. The BE for the Nb $3d_{5/2}$ shell in the case of Nb-KIT-6 (208.1 eV) was found to be higher than the corresponding Nb_2O_5 oxide (207.3 eV).[33] Moreover, the oxidation state of the Nb in the bimetallic Mo/Nb sample yielded a single Nb 3d doublet at ~207.8 eV ($3d_{5/2}$) and ~210.4 eV ($3d_{3/2}$) (Figure S4f). These features are characteristic of a Nb (+5) oxidation state in a surrounding oxide, similar to pure Nb_2O_5.[28] Additionally, the BE values of the Nb $3d_{5/2}$ in the bimetallic Mo/Nb the BE was found to increase with decreasing Nb content (207.1 to 208.5 eV) (Table S2). Such a shift towards higher BE values is an indication of increased dispersion of the Nb species on the silica support, likely due a change

in the coordination environment of the Nb through the formation of highly dispersed Nb-O-Si species. In other words, the surface niobia species (NbO_x) are highly isolated (Nb-O-Si) with no Nb-O-Nb interaction as also evident via TEM and DR UV-Vis (E_g = 5.5 eV, Table S6) results. Further, the metal dispersion on various catalysts was estimated from the surface atomic concentrations (%) of the Mo species and the dopant metals based on the XPS intensity ratios (Table S3). Despite identical Mo loadings in Mo_2/KIT-6 and $Mo_2/Nb_{1.5}$-KIT-6 catalysts, Mo is almost two times more abundant on the surface of the MoNb catalyst (~1.5) compared to the unpromoted catalyst (~0.8). These results are consistent with TEM results, confirming that Nb addition leads to the increased dispersion of the Mo species compared to other dopant promoter metals (MoNb > MoTa >MoZr > MoHf > Mo).

3.2 Comparative metathesis activity of monometallic and bimetallic catalysts

3.2.1 Rate measurements at differential conditions

For similar Mo (~2 wt%) loadings, the catalytic performances of monometallic Mo_2/KIT-6 (WI), as well as the bimetallic $Mo_2/M_{1.5}$-KIT-6 ($Mo_2/M_{1.5}$) catalysts, are compared under differential ($X_{2\text{-butene}}$ <10%) conditions (Figure 1a). The initial propylene formation rates on the catalyst samples were measured at various space velocities [WHSV = 4 - 18.2 $mol_{feed}/(mol_{Mo}\ s)$] under similar reaction conditions [n(ethylene)/n(2-butene)/Argon in feed = 3/1/4 molar ratio, 1 atm, 450 °C, $X_{2\text{-butene}}$ <10%]. The Mo_2/KIT-6 catalyst provided initial propylene formation rates of 28.7 ± 1.1 mmol $(mol_{Mo}\ s)^{-1}$. In contrast, incorporating ~1.5 wt% of the second metal (Nb, Ta, Zr or Hf) increases the propylene formation rates to 54.2 ± 0.5 mmol $(mol_{Mo}\ s)^{-1}$ with Nb, followed by 48.2 ± 0.6% with Ta, 43.5 ± 1.2 mmol $(mol_{Mo}\ s)^{-1}$ with Zr, and 37.6 ± 0.9 mmol $(mol_{Mo}\ s)^{-1}$ with Hf (Figure 1a, Table S4). Thus, all the tested group IV and V metals promote the metathesis activity. The propylene formation rates over Mo_2/KIT-6 and $Mo_2/Nb_{1.5}$-KIT-6 ($Mo_2/Nb_{1.5}$)

catalysts showed steady activity even after 24 h time on stream (TOS) (Figure S5). Note that the 2-butene to 1-butene isomerization rates are significantly faster on both these catalysts compared to the propylene formation rates (Figure S6 (a,b)).

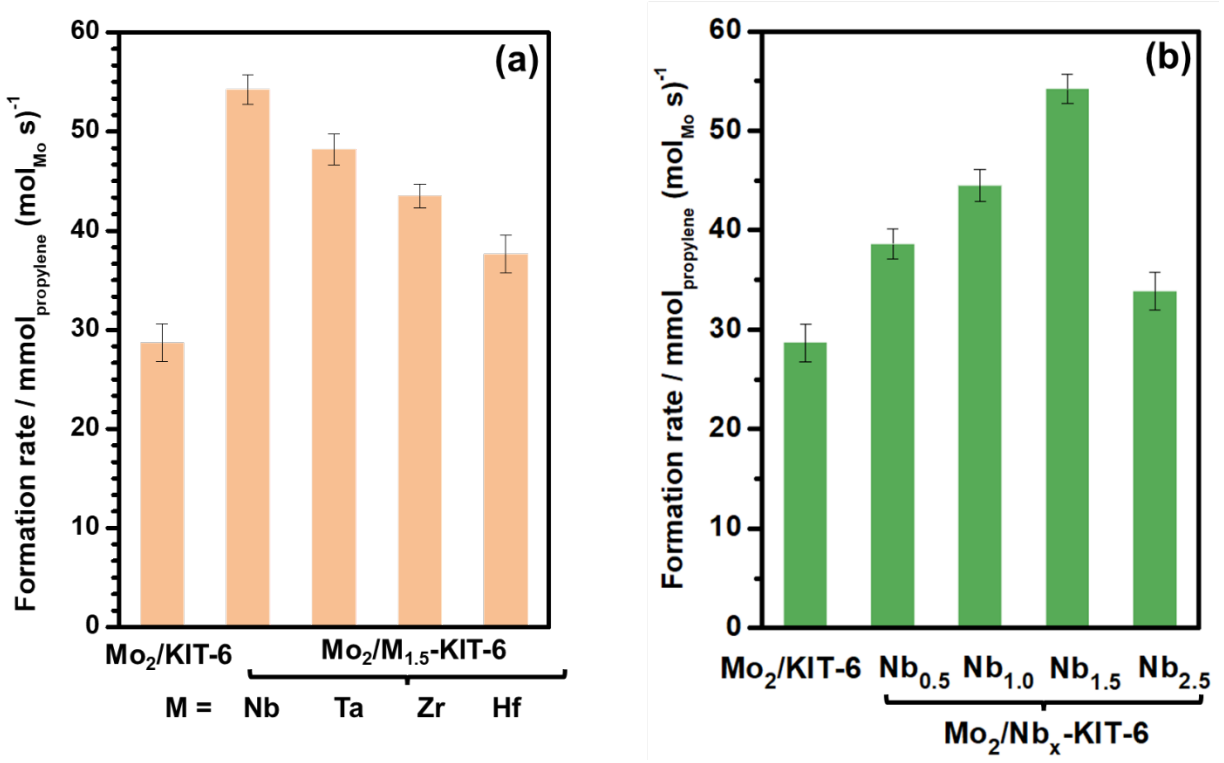

Figure 1. (a) Initial propylene formation rates for Mo_2/KIT-6 and $Mo_2/M_{1.5}$ KIT-6 catalysts, **(b)** Effect of Nb loadings on the initial propylene formation rates of the Mo_2/Nb_x-KIT-6 catalysts. Reaction conditions**:** T= 450 °C, P = 1 atm, WHSV (ethylene+2-butene+Argon) = 4-18.2 $mol_{feed}/(mol_{Mo}$ s), n(ethylene)/n(2-butene)/Argon in feed = 3/1/4 molar ratio, catalyst amount = 50 mg, , SiC = 2 g, particle size = 300 µm, with ethylene and 2-butene conversion <10%.

We also evaluated the catalytic performances of the supports ($M_{1.5}$-KIT-6) as well as physical admixtures of $M_{1.5}$-KIT-6 and Mo_2/KIT-6 (Table S4). While the $M_{1.5}$-KIT-6 supports show some activity for 2-butene to 1-butene isomerization, they do not exhibit metathesis activity in the absence of Mo species. Further, physical admixtures yielded propylene formation rates identical to those afforded by the Mo_2/KIT-6 catalysts alone. These results suggest that the dopant metal (M), support and the Mo metal act in synergy to create additional active metathesis precatalytic

sites. We hypothesize that the observed activity on the bimetallic formulation stems from reactions occurring on two types of sites: the traditional Mo dioxo species prevalent on the monometallic precatalyst, viz, $(O=)_2Mo(-O-Si)_2$ species as well as the newly formed bimetallic precatalysts $(O=)_2Mo(-O-M)(-O-Si)$ where the metal center is coordinated to the M-O-Si framework as isolated metal sites (Scheme 1). It must be noted that while the concentrations of the promoter metal (Nb) and active metal (Mo) are similar (ca. 1.5-2 wt%), only a small fraction of the promoter metal sites within the silica framework are accessible for the formation of adjacent, precatalytic sites ($((O=)_2Mo(-O-Nb)(-O-Si))$. Hence, we also refer to the metal promoters as dopants in this study.

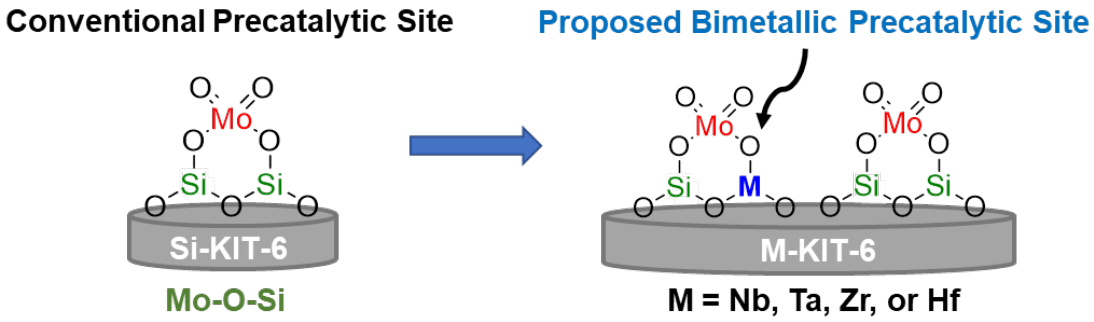

Scheme 1. Proposed dioxo surface Mo pre-catalyst present on $Mo_2/M_{1.5}$-KIT-6 support.

We also investigated the effect of Nb loadings on the metathesis activity of Mo_2/Nb_y-KIT-6 (y = 0.5-2.5 wt%) under identical reaction conditions (Figure 1b). The $Mo_2/Nb_{1.5}$-KIT-6 catalyst with a Nb loading of ~1.5 wt% provides the highest propylene formation rates [54.2 ± 0.5 mmol $(mol_{Mo}\ s)^{-1}$]. At higher Nb loadings (~2.5 wt%), these values decrease [33.9 ± 1.9 mmol $(mol_{Mo}\ s)^{-1}$] and are closer to those observed for the monometallic Mo_2-KIT-6 catalyst [28.7 ± 1.1 mmol $(mol_{Mo}\ s)^{-1}$]. At the lower Nb loadings (~0.5 wt%), the metathesis activity of the bimetallic catalyst did not show appreciable improvement [38.6 ± 0.6 mmol $(mol_{Mo}\ s)^{-1}$]. These observations suggest the existence of an optimum Nb loading at which the number of adjacent Mo-O-Si and Mo-O-Nb sites required to form the new precatalytic sites is maximized.

3.2.2 Integral conversion data

The effects of reactor residence time on product formation rates were investigated under integral reaction conditions [WHSV = 0.8-6 h^{-1}, n(ethylene)/n(2-butene) = 3/1, 1 atm, 450 °C]. We conducted catalytic tests employing pure 2-butene as the feed. The 2-butene conversion (~65%) and the 1-butene yield (~11%) remained constant at all space velocities (0.8-6 h^{-1}) (Figure S7 (a,b)). Further, the isomerization activity when co-feeding ethylene and 2-butene (molar ratio = 3:1) was nearly constant (1-butene yield ~16%) at all residence times (0.2-1 h g_{Mo} g_{feed}^{-1}), suggesting that the 2-butene isomerization attends equilibrium rapidly on Mo-supported monometallic catalysts (Figure S8 (a,b)). However, upon Nb addition ($Mo_2/Nb_{1.5}$), the 2-butene conversion increased from 56% to 62% and propylene selectivity increased from 66% to 74%, while the 1-butene selectivity decreased from 30% to 22% (Figure S8c, Table S5). We postulate that mixed MoO_4, MoO_6, and MoO_3 species are responsible for isomerization activity while the conventional precatalyst $(O=)_2Mo(\text{-}O\text{-}Si)_2$ species and the additional bimetallic Mo/M-KIT-6 $((O=)_2Mo(\text{-}O\text{-}M)(\text{-}O\text{-}Si)$ species are responsible for the metathesis activity (see Sec. SC1, Scheme S1).

3.3 Catalyst stability and regenerability

To test the catalyst stability under integral conditions, the apparent propylene formation rates ($mole_{propylene}/mol_{Mo}$ h), also expressed as the space-time yield (STY, h^{-1}) evaluated at the steady-state values calculated between 0.3 h and 7 h, indicate that the $Mo_2/Nb_{1.5}$ catalyst is the most active. The reactivity order is as follows: $Mo_2/Nb_{1.5}$ (32.7 h^{-1}) > $Mo_2/Zr_{1.5}$ (28.2 h^{-1}) > $Mo_2/Ta_{1.5}$ (27.2 h^{-1}) > $Mo_2/Hf_{1.5}$ (25.7 h^{-1}) > Mo_2/KIT-6 (22.9 h^{-1}) (Figure S9). Similar enhancement was also observed with $Mo_2/Nb_{1.5}$-KIT-6 catalyst prepared in a different batch (Figure S10), confirming reproducibility. Post-reaction analysis of the spent catalyst suggests that the minor deactivation is

reversible and is likely due to coke formation and some adsorbed olefins that participate during the reaction cycle, as evidenced by XPS, TGA, and ^{13}C ssNMR analysis (Figures S11-S13). Further, the metathesis activity of the spent $Mo_2/Nb_{1.5}$-KIT-6 catalyst is restored by regeneration in flowing air (100 sccm) at 550 °C for 5 h (Figure S14). The observed propylene formation rate on the $Mo_2/Nb_{1.5}$ catalyst is significantly higher (~5-10 fold) than those reported for the Mo-based catalysts on modified supports,[10, 30, 31] but similar to those reported on Siral supports[34] at 50 °C. It is unclear if the reported rates on Siral supports are steady. It must be noted that the foregoing comparisons are to be treated with due caution as the reaction conditions, and therefore the intrinsic reaction and catalyst deactivation mechanisms, are different for the various catalysts. We confirmed that the Mo_2/KIT-6, $Mo_2/Nb_{1.5}$-KIT-6, and $Mo_7/Nb_{1.5}$-KIT-6 catalysts do not show any appreciable activity for propylene formation at ~50 °C. In general, our observations from *in situ* DRIFTS experiments suggest that a higher temperature is needed to activate the Mo-carbene species and to ensure either no or only weak participation of the surface hydroxyl silanols,[35] allowing facile product desorption during the metathesis reaction (Section SD1.4, Figure S15 (a,b)). To corroborate this, we investigated the effect of reaction temperature (300-450 °C) on the metathesis activity (Figure S16 (a,b)). As expected, the overall 2-butene conversion decreases at lower temperatures. However, the selectivity towards 1-butene becomes comparable to propylene formation at lower temperatures wherein the 2-Butene ↔ 1-Butene equilibrium conversion is favored relative to higher temperatures. Hence, we chose to operate at 450 °C wherein the metathesis precatalytic sites (O=Mo=O, dioxo Mo sites) are more active compared to other surface Mo species (oligomers, bulk).

3.4 Coordination environment of Mo sites

The nature and the identity of the surface Mo species were investigated by several characterization techniques. The local coordination environment of the surface MoO_x species on the supported catalysts was probed with DR UV-Vis spectroscopy as shown in (Figures 2a and S17). Under hydrated conditions, both the Mo_2/KIT-6 and the bimetallic $Mo_2/M_{1.5}$-KIT-6 catalysts possess two ligand-to-metal charge transfer (LMCT) transition ($O^{2-} \rightarrow Mo^{6+}$) with a band maxima at ~250 nm attributed to isolated monomeric Mo species, and another band at ~310 nm attributed to oligomeric species (Mo-O-Mo) are consistent with those reported by previous researchers studying metal oxide supported Mo catalysts, including for metathesis applications.[36-39] The absence of d-d band around ~360-400 nm (present in Mo_2/KIT-6, Figure 2a) in the case of bimetallic $Mo_2/M_{1.5}$-KIT-6 catalysts suggests that the MoO_x species (Mo^{VI}) on the promoted catalysts are highly dispersed, consistent with the findings from the wide-angle XRD (Figure S1) and TEM analysis (Figure S3). The broad nature of the absorption bands and the significant overlap in the spectral regions resulting from several excitations[39, 40] have been interpreted employing theoretical approaches such as time-dependent density functional theory (TD-DFT) calculations.[41, 42] Sanchez et al.[43] employed TD-DFT for Ti-zeolite (TS-1) and Ti-containing silica (Ti/SiO_2) catalysts to demonstrate agreement between calculated electronic transitions and the experimental UV-Vis spectra. Their calculations demonstrate that an increase in the coordination number of Ti-sites leads to peak broadening, showing clear demarcations between isolated tetrahedral and octahedral Ti sites. To our knowledge, similar theoretical calculations are not available for Mo-supported catalysts. Nevertheless, by comparison with standard molybdenum compounds (such as sodium molybdate, ammonium heptamolybdate and molybdenum oxide), a generalized interpretation can be made. The DR UV-Vis spectra for all the Mo-supported catalysts under

hydrated conditions reveal an additional peak maxima at higher wavelengths (>300 nm) as compared to the spectrum of Na_2MoO_4 (~250 nm and 260 nm for isolated four-coordinated monomeric species),[39, 44] suggesting the presence of an additional species, possibly oligomeric MoO_x species. Moreover, the centers of the two absorption bands (250 and 310 nm, corresponding to 4.96 and 4.00 eV, respectively) are separated by about ~1 eV. This gap appears significant enough to be the difference between the split energy levels of the metal center's d bands suggesting that the absorption bands are associated with different species.[45] Further, the bimetallic catalysts ($Mo_2/M_{1.5}$-KIT-6) show higher edge energy (E_g) values (~3.8-3.9 eV) compared to Mo_2/KIT-6 catalysts (~3.2 eV) consistent with the LMCT deconvolution results showing qualitatively a higher proportion of isolated four-coordinated monomeric species upon the addition of dopant metals (Table S6, Figure S18 (a-e)).[46-49] We also employed XANES and EXAFS to gain additional insights into the local Mo structures in the catalysts.

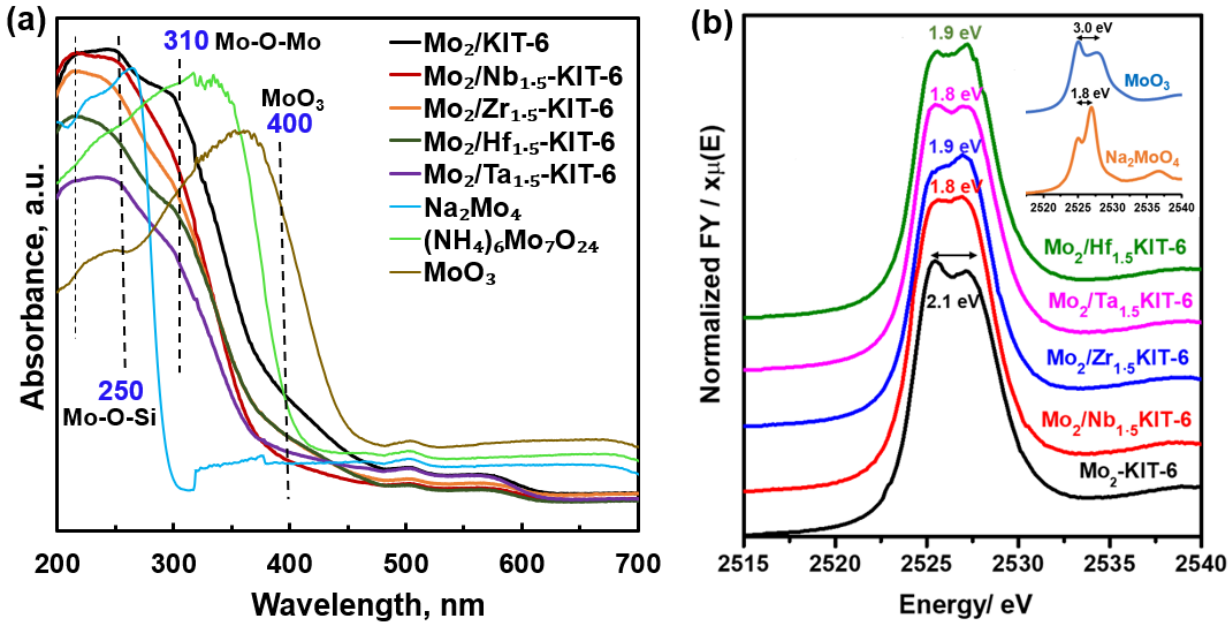

Figure 2. (a) Diffuse reflectance UV-Vis spectra of the fresh Mo_2/KIT-6, $Mo_2/M_{1.5}$-KIT-6 catalysts with dopants (M = Nb, Zr, Ta, Hf), with reference compounds Na_2MoO_4, $(NH_4)_6Mo_7O_{24}$, and at MoO_3 at ambient temperature (25 °C), **(b)** Normalized fluorescence yield (FY) Mo L_3-edge

XANES spectra of the hydrated supported monometallic and bimetallic Mo-based catalysts, with reference compounds Na_2MoO_4 and MoO_3 (inset) at ambient temperature (25 °C).

Mo L_3-edge XANES was employed to investigate the difference in the local site symmetry of MoO_x species arising from the metal-support interactions on monometallic and bimetallic catalysts. Mo L_3-edge XANES is sensitive to the coordination environment of Mo center, as it involves the dipole-allowed 2p → 4d transition, and thus the edge position reflects the local oxidation state.[50, 51] All the samples show a double featured white line peaks (Figure 2b) originating from the ligand field splitting of 1.8-2.1 eV for the *d* orbitals of the Mo.[50, 52, 53] Compared to monometallic Mo_2/KIT-6 catalyst, for all the bimetallic catalysts ($Mo_2/M_{1.5}$-KIT-6), the relative intensity ratios between the two white lines are consistent and higher for all the bimetallic catalysts ($Mo_2/M_{1.5}$-KIT-6), suggesting that more MoO_x species exist in four coordinated tetrahedral rather than octahedral coordination.[39, 41, 42] This is consistent with DR UV-Vis spectroscopy results. On the other hand, in Mo K-edge XANES, since the octahedral Mo in MoO_3 exists in off-centered asymmetric locations, both octahedral and tetrahedral Mo allow 1s-to-4d transition that results in the pre-edge feature.[44, 54] Therefore, the pre-edge feature exists in the K-edge XANES of all samples, monometallic or bimetallic, as well as that of bulk MoO_3 (Figure 3a). For all samples, the Mo K-edge energies at the first maximum is close to that of MoO_3 standard, suggesting the Mo oxidation state of around +6 on the samples.[44]

3.5 Molecular structure of the surface MoO_x species

The molecular structure and speciation of the supported MoO_x species on different oxide supports have been extensively studied using *in situ* Raman and XAS spectroscopies, with their structural assignments facilitated by theoretical calculations.[18, 52, 53, 55] The *in situ* Raman spectra of supported Mo_2/KIT-6 and the $Mo_2/M_{1.5}$-KIT-6 catalysts under dehydrated conditions (He flow

of 40 sccm, 450 °C) are presented in Figure 3b. All the supported catalysts exhibit a broad peak centered around 957-965 cm^{-1} assigned to the asymmetric stretch of the isolated dioxo surface species ($\nu_{as}(O=)_2MoO_2$).[48, 56-58] The shifts observed from 947 cm^{-1} under hydrated conditions (Figure S19) to 965 cm^{-1} under dehydrated conditions (Figure 3b) suggest that isolated monomeric Mo dioxo $(O=)_2Mo(-O-Si)_2$ species are favored over polymolybdate species on the bimetallic catalysts. In addition, a very weak band at 1020-1030 cm^{-1} for the dehydrated Mo_2/KIT-6 is attributed to the formation of isolated monoxo Mo species $O=Mo(-O-Si)_4$ which coexists in equilibrium with isolated dioxo species (~957 cm^{-1}). These observations are consistent with DFT calculations reported for the formation of surface monoxo MoO_5 species on amorphous silica supports.[57, 59] The weak and broad bands observed between 825-878 cm^{-1} in Mo_2/KIT-6 and $Mo_2/M_{1.5}$-KIT-6 (M = Nb, Zr, Hf, or Ta) materials are assigned to the bridging Mo-O-Mo and/or Mo-O-M bonds.[52, 60] Under dehydrated conditions, a small band at ~818 cm^{-1}, attributed to crystalline MoO_3 NPs, is observed in the case of Mo_2/KIT-6 materials consistent with results from DR UV-Vis spectra (ambient conditions, E_g = 3.2 eV, Table S6) for this material. However, this band is not as well defined in the bimetallic catalysts suggesting that the surface MoO_x species in these materials are so well dispersed that they avoid sensitive detection. Thus, the results from Raman spectroscopy are generally in agreement with the DR UV Vis spectra while providing more insights into the nature of the major surface species on the bimetallic catalysts.

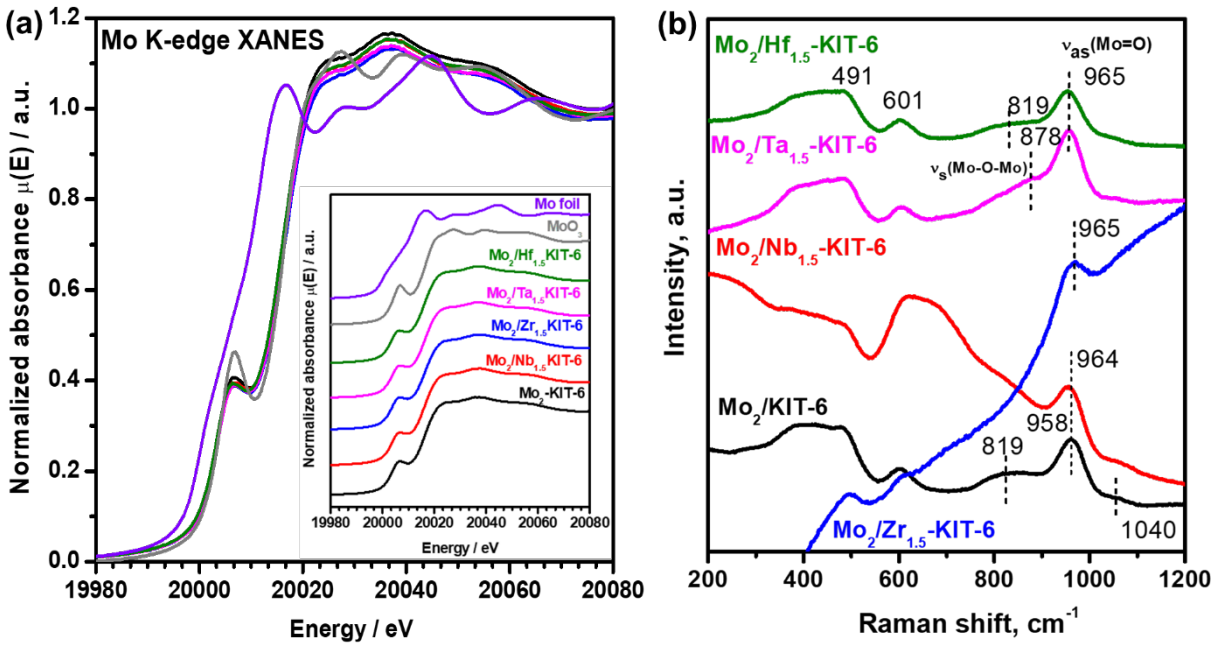

Figure 3. **(a)** Comparison of Mo K-edge normalized XANES spectra of the hydrated supported monometallic, bimetallic Mo-based catalyst, and MoO_3 standard compound with Mo foil as reference. All the measurements are performed under ambient conditions (25 °C); **(b)** Raman spectra of the supported Mo_2/KIT-6 and bimetallic $Mo_2/M_{1.5}$-KIT-6 catalysts under dehydrated conditions, 450 °C.

The k^2-weighted Mo K-edge EXAFS of hydrated Mo_2/KIT-6 and $Mo_2/Nb_{1.5}$-KIT-6 samples are shown in Figure S20 (k-space and R-space magnitude, collected at 25 °C), with the fitting shown in dashed lines and the fitting parameters shown as Table S7. The best model to describe the EXAFS of both samples includes three types of Mo−O scattering paths in the crystal structure of MoO_3 (R ~ 1.70, 1.98, and 2.30 Å, respectively), the Mo−Si and Mo−Mo non-bonding scattering paths (R ~ 3.35 and 3.79 Å, respectively), as well as all multiple scattering paths associated with them (refer to SI, Section SE1.3 after Table S7 for detailed description). Such a model is consistent with a mixture of Mo four-coordinated monomers, oligomers and/or small clusters supported on SiO_2,[53, 57] the proposed structure based on UV-Vis, XANES and Raman results. We note that EXAFS analysis cannot effectively differentiate between the two types of Mo species because the

shortest two Mo-O bonds in octahedral environment has similar length (e.g., 1.76 Å in MoO_3) with the two Mo=O bonds in tetrahedral environment (~1.72 Å in the literature[56, 57, 61]). It cannot differentiate Mo-O-Nb from Mo-O-Mo structures either due to the close atomic number of Mo (42) and Nb (41). As a result, the EXAFS of the two samples and fitting parameters are highly similar despite the structural difference suggested by UV-Vis and Raman. For the same reason, the EXAFS of other bimetallic catalysts (Figure S21) does not vary significantly either.

Thus, Raman spectroscopy, DR UV-Vis, XANES, and EXAFS results together provide a better understanding of the structure of the surface MoO_x species suggesting that majority of the Mo sites exist as isolated monomeric four-cordinated Mo dioxo species on $Mo_2/Nb_{1.5}$-KIT-6 catalyst. The extracted (Mo=O) bond distances are consistent with the structure of dioxo molybdates $(O=)_2Mo(-OSi)_2$[56, 57] with a minor concentration of oligomeric MoO_x species. Similar dioxo molybdates species were observed for the supported Mo catalysts prepared using two different synthesis techniques adding credence to our findings.[62] Although the proposed bimetallic structures have similar Mo dioxo surface sites, the marked difference in the metathesis activity with different dopant metal (MoNb > MoTa > MoZr > MoHf > Mo), further led us to investigate the electronic structure and strength of the Lewis acidic metal center in the bimetallic catalysts. Such investigations reveal that, depending on the dopant, different types of active site precatalysts are distinguishable on the catalyst surface, each giving rise to different extent of activity enhancement.

3.6 Strength of Lewis and Brønsted Acid Sites

The *in situ* diffuse reflectance FTIR (DRIFTS) spectra of the $M_{1.5}$-KIT-6, Mo_2/KIT-6, and $Mo_2/M_{1.5}$-KIT-6 catalysts obtained during temperature programmed desorption (TPD) of adsorbed pyridine in flowing He (~0.1 kPa pyridine, 40 sccm) between 150-300 °C are shown in Figures 4 and S22. Both the support and the Mo doped catalyst contain predominantly Lewis acid sites, as

inferred from the strong peak at ~1448 cm^{-1} and 1608 cm^{-1} respectively, with one additional band at 1595 cm^{-1}.[15, 16] Interestingly, this latter band was more prominent and well resolved in the bare transition supports (M-KIT-6) and its intensity decreased upon Mo incorporation with a simultaneous increase in the intensity of the vibrational band at 1608 cm^{-1} (Figure S22). Such an interaction could be possibly due to the presence of different strengths of electrophilic Lewis acid sites which are characteristic of transition metals (Group IV and V). Additionally, the peak around 1540 cm^{-1}, corresponding to Brønsted acid sites, is relatively small for the $Mo_2/M_{1.5}$-KIT-6 catalyst.[15] Coordinatively unsaturated monomeric Mo^{VI} di-oxo species have been reported to be the precatalytic active sites for carbene formation in metathesis[8, 9, 11, 13] and exhibit Lewis acidity while the surface silanols in close proximity to the monomeric Mo^{VI} metal centers exhibit Brønsted acidity.[63, 64]

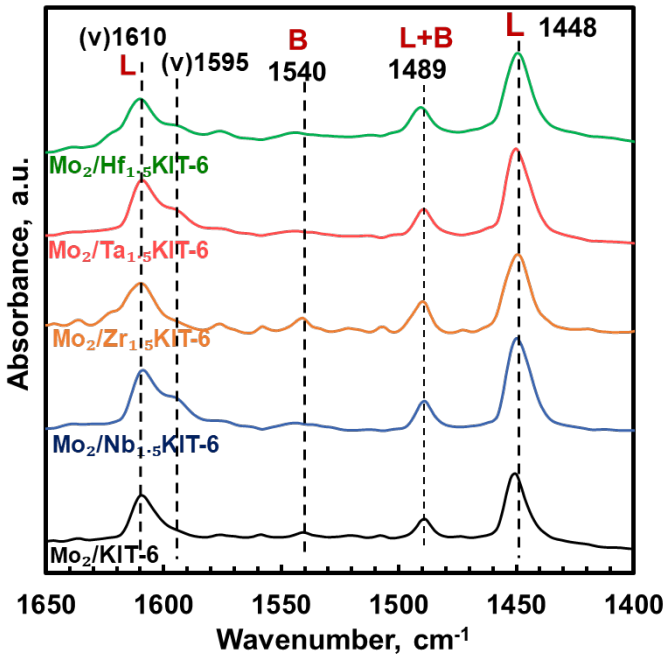

Figure 4. In situ Py-IR of Mo_2/KIT-6 and $Mo_2/M_{1.5}$-KIT-6 samples at 150 °C. The plots are obtained after subtraction of desorbed pyridine spectra at 150 °C from the dehydrated sample spectra prior to pyridine absorption at 150 °C; L- Lewis and B- Brønsted acid sites.

Additionally, these catalysts possess acid sites of moderate strength as indicated by the desorption occurring in the temperature range of 200-300 °C, consistent with NH_3-TPD results (Figure S23). The TPD-pyridine spectra (Figure S24 (a-d)) show that the normalized Lewis acid band areas at ~1448 cm^{-1} on the doped silicate materials ($M_{1.5}$-KIT-6) are nearly identical to those observed in the presence of Mo ($Mo_2/M_{1.5}$-KIT-6). While the Lewis acid sites in the $M_{1.5}$-KIT-6 and the corresponding $Mo_2/M_{1.5}$-KIT-6 materials are of similar strength, they vary with different dopant metals (Figure S25 (a,b)). As inferred from NH_3-TPD acidity values (Table S1), the addition of Mo species to the $Mo_2/M_{1.5}$-KIT-6 catalyst affects only the density of acid sites. Thus, the pyridine band areas calculated for the $M_{1.5}$-KIT-6 supports, and the $Mo_2/M_{1.5}$-KIT-6 catalysts are appropriate to quantify the relative strengths of Lewis acid sites on the various bimetallic catalysts.

The enthalpy of pyridine adsorption ($\Delta H_{ads,py}$), a measure of the relative strengths of the acid site, has been widely reported.[65-67] The adsorption enthalpies ($\Delta H_{ads,py}$) are determined from the pyridine adsorption isobars (0.1 kPa, 175-300 °C) at steady-state conditions by evaluating the normalized Lewis acid band areas of the pyridine (at ν=1448 cm^{-1}) and regressing these values to the van't Hoff equation (Figure S25b). The values of the adsorption enthalpies ($\Delta H_{ads,py}$), summarized in Table S8, indicate that the interaction of pyridine with isolated Nb^V is the most exothermic and strongest among M sites, with the Lewis acid strength decreasing in the order Nb > Ta > Zr > Hf.

3.7 ^{1}H MAS ssNMR of adsorbed pyridine-d_5

The ^{1}H MAS ssNMR spectra provide information on the presence of different surface hydroxyl groups and their accessibility to the guest molecules, adsorbed moisture and proton exchange processes occurring on the silica surfaces.[68, 69] The ^{1}H NMR spectra of the fresh and dehydrated

$Mo_2/M_{1.5}$-KIT-6 catalysts (Figure S26a) consist of an intense signal resonating at ~2.4 ppm assigned to isolated silanol groups.[25, 70] Compared to the Mo_2/KIT-6 catalyst, the bimetallic $Mo_2/M_{1.5}$-KIT-6 catalysts show a weak shoulder peak at ~3.2-3.5 ppm assigned to the hydrogen-bonded silanols at ambient conditions. Deuterated pyridine (Py-d_5) was employed as a probe molecule to determine the nature and strength of newly formed surface acidic sites resulting from the interaction with different metal (M) sites. In the presence of deuterated pyridine (pyridine-d_5), shown in Figure 5a, the ^{1}H MAS NMR of the isolated silanol signal at ~2.4 ppm shifts to ~10.1 ppm, indicating the formation of a hydrogen bond between the pyridine and the non-acidic silanols, similar to those observed in zeolites and mesoporous silica.[71, 72] The new chemical shifts at ca. 7.5, 7.9, 8.2, and 9 ppm are assigned to the residual aromatic protons of the pyridine (Figure 5a).[25] In particular, the shift of signals to a lower field (7-9 ppm) in all the catalysts suggests that the strength of the acidic OH sites are weak, perhaps similar to those on $M_{1.5}$-KIT-6 (Figure S26b) and not adequate to protonate the pyridine molecule (hydrogen-bonded pyridines).[73]

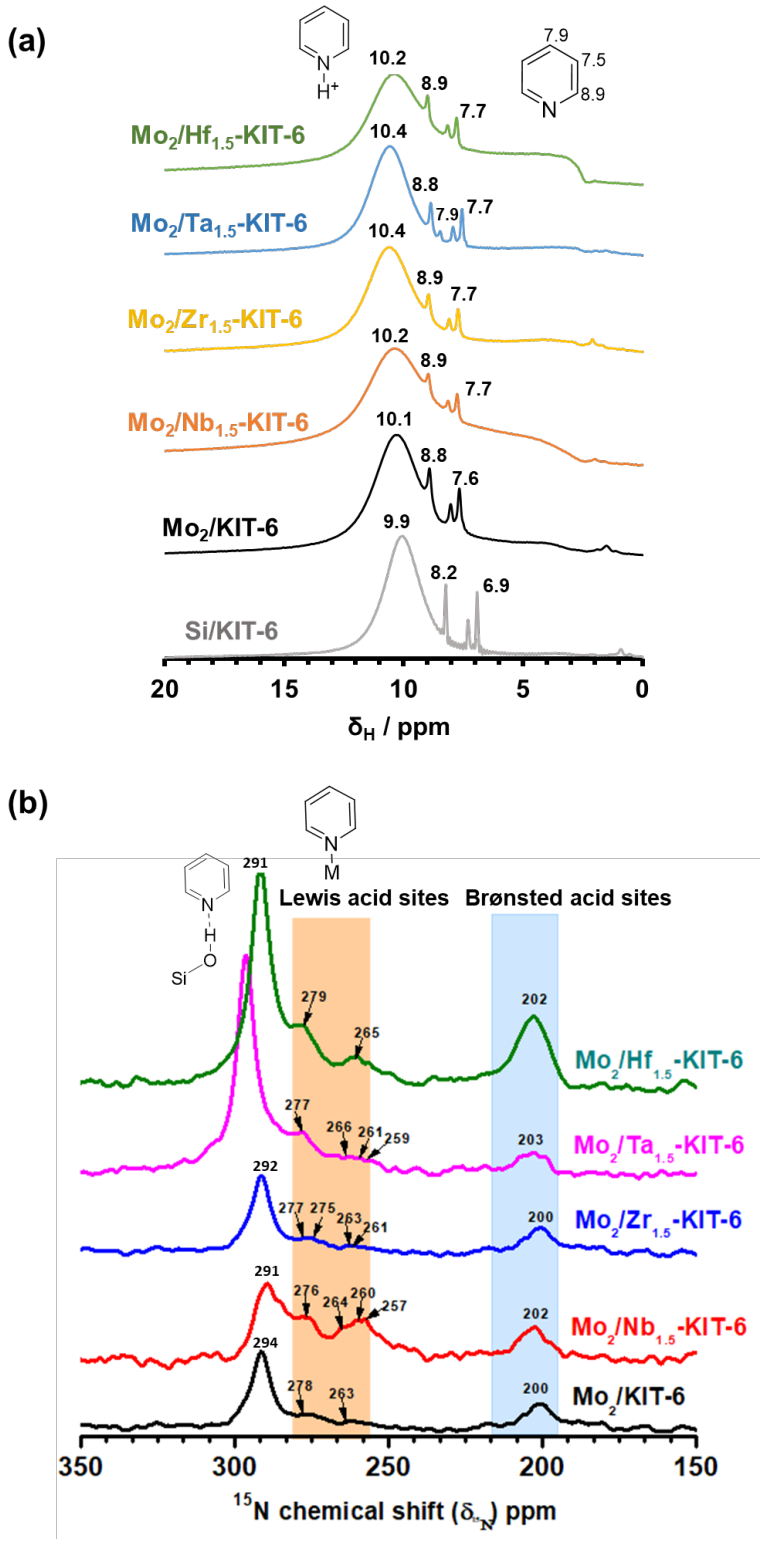

Figure 5. (a) ^{1}H MAS ssNMR spectra of the fresh and dehydrated Mo_2/KIT-6 and $Mo_2/M_{1.5}$-KIT-6 catalysts adsorbed with deuterated pyridine-d_5, **(b)** ^{15}N CP MAS ssNMR spectra of the ^{15}N-pyridine adsorbed on fresh and dehydrated $Mo_2/M_{1.5}$-KIT-6 catalysts.

3.8 ^{15}N CP MAS ssNMR of adsorbed ^{15}N-pyridine

^{15}N solid-state NMR of the adsorbed ^{15}N-pyridine is a useful technique to probe the acid character of metal-substituted mesoporous silicates and zeolites.[25, 68, 72, 74, 75] In particular, both Lewis and Brønsted acid sites are distinguishable using Py-IR and ^{15}N ssNMR techniques. The Py-IR technique cannot distinguish between the pyridine coordinated to the metal center, weak Brønsted acid site or metal coordinated to the surface hydroxyl groups (MOH). In contrast, ^{15}N ssNMR can differentiate different metal centers or structures from weak Brønsted acid sites. The chemical shift (δ) of the free pyridine is observed at around 320 ppm. The peak moves up by 10-50 ppm when the nitrogen of the pyridine molecule is coordinated to the Lewis acid site (230 – 280 ppm) and attains a value of ~200 - 210 ppm when interacting with Brønsted acid site[62, 76], yielding a 110 ppm chemical shift range that can be used to distinguish the type and strength of acid sites.[75, 76]

The ^{15}N CP MAS ssNMR spectra of the fresh and dehydrated $M_{1.5}$-KIT-6, Mo_2/KIT-6 and $Mo_2/M_{1.5}$-KIT-6 catalysts adsorbed with ^{15}N-pyridine, shown in Figure S27 and Figure 5b, reveal the absence of weakly physisorbed pyridine at around 315-325 ppm[76, 77] In the case of Si-KIT-6, the chemical shift at ~298 and 288 ppm are assigned to isolated silanols and weakly interacting hydrogen bonded silanols[25, 78, 79] (Figure S27), consistent with the observations from ^{1}H MAS NMR spectra (Figure S26a). For the transition metal supports ($M_{1.5}$-KIT-6), the signal for the isolated silanols at ~298 ppm is shifted to ~290-288 ppm due to the interaction of the silanols with pyridine (H-bonded pyridine).[62] The chemical shifts (δ) of the adsorbed ^{15}N-pyridine on Nb and Ta show intermediate chemical shifts at 276 and 268 ppm assigned to pyridine coordinated to the Lewis acid site (coordinated to metal centers). Zr and Hf also show similar resonances at 277 and 278 ppm associated with the pyridine adsorbed on Lewis acid sites.[25, 76, 80] The Zr-KIT-6 sample

also exhibited a small resonance shift at ~205 ppm associated with strong Brønsted acidity similar to those observed in sulfated zirconia catalysts.[81] The introduction of the Mo species in the $Mo_2/M_{1.5}$-KIT-6 catalysts further shifted, albeit slightly, the values to ~291 ppm suggesting even stronger interaction with the silanol species (Figure 5b). Further, some Brønsted acidity was also induced in all the $Mo_2/M_{1.5}$-KIT-6 catalysts, as evidenced by a resonance shift for the protonated pyridine at ~202 ppm, with the intensity corresponding to the MoHf catalysts being the highest. The chemical shifts observed at 257, 259, 264 and 265 ppm for the $Mo_2/M_{1.5}$-KIT-6 catalysts are not observed either on the bare supports or Mo_2/KIT-6 catalyst suggesting the formation of Lewis acid sites (coordinated to Mo centers) with different strengths on the $Mo_2/M_{1.5}$-KIT-6 catalysts. Thus, the observed variations in the ^{15}N chemical shift (δ) are attributed to the different geometric and coordination environments of structurally similar Mo dioxo sites (precatalysts) which in turn tune the metathesis activity. The coordination of the Mo metal with the M-O-Si framework during the one-pot synthesis aids the formation of new Mo-O-M active site pre-catalyst that we hypothesize as being responsible for enhancing the olefin metathesis activity. Similar cooperative catalysis effect has been observed with the formation of W-O-Zr species in WZr-KIT-6 catalyst[25] and W-O-Sn species in WSn-KIT-6 catalyst.[26]

3.9 Relationship of Reactivity to Molecular and Electronic Structures

The *in situ* FTIR experiments of the adsorbed pyridine combined with temperature-programmed desorption reveals the presence of dominant Lewis acid in all the supports and bimetallic supported catalysts. The pyridine adsorption enthalpies ($\Delta H_{ads,py}$) associated with Lewis acid sites (M) thus provides a direct and quantitative measure of the strength for all the $M_{1.5}$-KIT-6 catalysts. The values of the adsorption enthalpies ($\Delta H_{ads,py}$) summarized in Table S8 indicate that the interaction of pyridine with isolated Nb^V is the most exothermic and strongest among M

sites, with the Lewis acidic strength decreasing in the order (Nb > Ta > Zr > Hf). The positive correlation between the propylene formation rates and the ($\Delta H_{ads,py}$) values suggests greater stabilization of the adsorbed olefins as the Lewis acid strength increases (Figure 6a). Additionally, the experimentally determined adsorption enthalpy also appears to correlate linearly with the Pauling's electronegativity values (EN). Strong Lewis acids such as niobium (Nb) possess the ability to extract the electrons from the nearest -(Mo-O)- moiety creating a charge imbalance and making the active Mo centers more electrophilic and reactive. This causes the electron density to change around the central Mo atom rendering the surface species (Mo=O) more reactive towards the electron rich species (C=C). Moreover, the presence of the Nb-O-Si ligand could introduce steric effects around the Mo=O bonds. These steric effects can influence the geometry of the Mo=O bonds, potentially affecting their electronic properties and reactivity.

We also investigated these electronic effects by taking a closer look at the binding energy values of Si 2p, O 1s and Nb 3d for the Nb-KIT-6 modified silica supports after Mo doping. Such an exercise provides valuable information on the coordination environment and molecular structure of the molybdenum species on these supports (Figures S28 and S29, Table S2). On bimetallic $Mo_2/Nb_{1.5}$ catalysts, the Si 2p and the O1s core-shell BE values shift to lower side (102.9 eV and 532.4 eV) compared to the bare $Nb_{1.5}$-KIT-6 support (103.5 eV and 532.9 eV) (Figure S29 (a,b)). This observation is explained by a slight decrease in the positive charge on the $Si^{\delta+}$ cation and a higher electron density on the oxygen atom, indicating a stronger covalency of the Si-O (EN difference = 1.54) bond in the oxide matrix. In comparsion, $Nb^{\delta+}$ is more electropositive (EN difference of Nb-O = 1.84), which makes the Nb-O bond more ionic. This leads to an excess positive charge on higher valent $Nb^{(V)}$ and induces Lewis acidity in the Nb-KIT-6 support. As $Nb^{\delta+}$ is more electron deficient, there will be coordination by the Mo-O-terminal of Mo(VI). Moreover,

the surface hydroxyls are more abundant on the niobia compared to silica and coordinate through the Nb-O and the adjacent Si-O to the Mo center of the Mo(VI). The latter (Si-O) represents a silanol group in close proximity to the metal site (silyl oxonium) such that the O is partially coordinated to the metal center, thus stabilizing the oxygen partial negative charge. A similar bidentate ligand model has also been reported for MoO_3/Al_2O_3-SiO_2, Mo/TiO_2-ZrO_2 and W/Al-Ti catalyst systems.[82-85] In the proposed model (Scheme 1), the four coordinated monomeric dioxo Mo species interact with the adjacent surface hydroxyl group to form the new bidentate species.

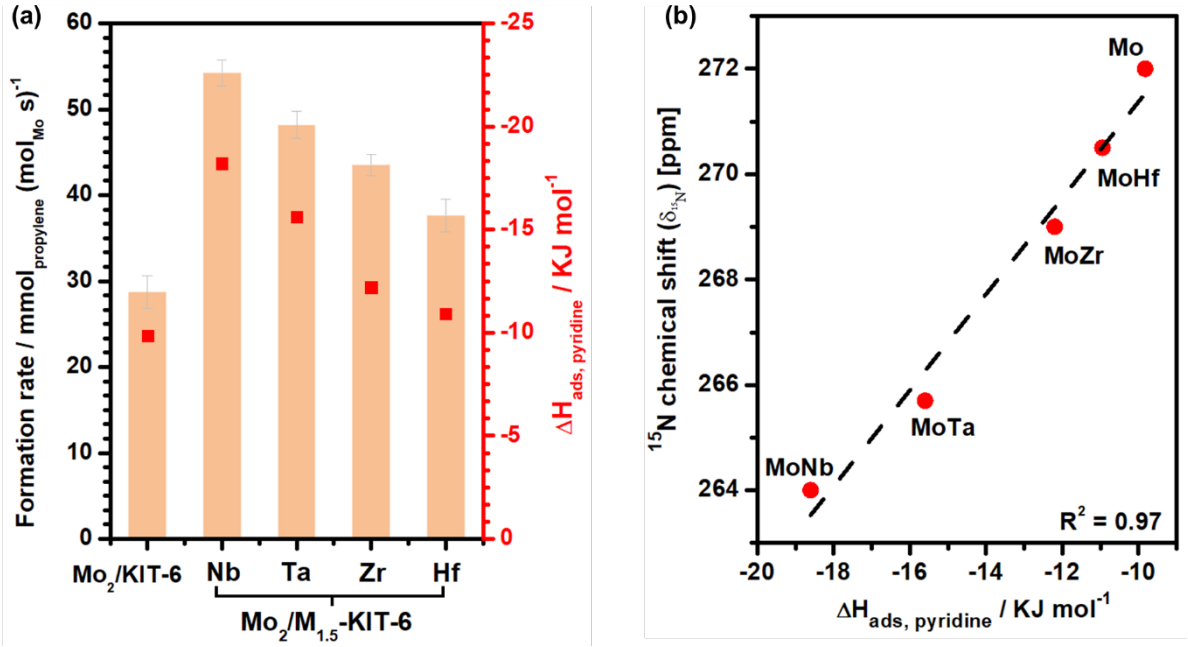

Figure 6. (a) Initial propylene formation rates for Mo_2/KIT-6 and $Mo_2/M_{1.5}$ KIT-6 catalysts and activity correlation with the pyridine adsorption enthalpies ($\Delta H_{ads,py}$) on the M-KIT-6 catalysts; **(b)** Correlation between the pyridine adsorption enthalpies ($\Delta H_{ads,py}$) and ^{15}N chemical shift (δ_{avg}) of the Py adsorbed to Nb, Ta, Zr, and Hf Lewis acidic metal centers.

Further, the average ^{15}N chemical shifts (δ_{avg}) determined for the various catalysts based on the averages of the chemical shifts observed over the 278 – 250 ppm range due to pyridine interaction with Lewis acid centers are sensitive to different electronic structure and coordination environments.[80, 86] The Mo/Nb catalysts showed the highest frequency shift, i.e., most intense Lewis

acid character, with ^{15}N average chemical shift (δ_{avg}) of 264 ppm, followed by Mo/Ta (265.7 ppm), Mo/Zr (269 ppm), Mo/Hf (270.5 ppm), and Mo_2/KIT-6 (~272 ppm). The observed trends are significant as they arise from the interaction of pyridine with the metal centers exhibiting distinct electronic states (Figure 5b). As such, with different support ligands, the occurrence of geometric strain affects the electronic properties of the Mo metal centers which could be linked to the reactivity.[87, 88] We show that a similar linear correlation also exists between the ^{15}N average chemical shifts (δ_{avg}) of the bimetallic catalysts ($Mo_2/M_{1.5}$-KIT-6) from the ^{15}N MAS NMR experiments and the Lewis acid strengths ($\Delta H_{ads,py}$) (Figure 6b). Previous studies involving different Lewis acid centers incorporated into zeolites and alumina supports showed similar linear correlations between the $\Delta H_{ads,py,}$ and the average chemical shifts of the ^{15}N adsorbed pyridine.[75, 76] Thus, the ^{15}N average chemical shifts help correlate the experimental activity measurements with the geometry, electronic structure and the metathesis activity of the Lewis acid metal centers in the precatalysts. However, in the case of weak Brønsted acid sites (OH sites) that are not strong enough to protonate the pyridine (as shown in ^1H NMR of $Mo_2/M_{1.5}$-KIT-6 catalysts adsorbed with pyridine-d_5, Figure 5a), the acidic strength has little influence on ^{15}N pyridine chemical shift. Hence the shift due to the pyridinium does not follow the same correlation.

4 CONCLUSIONS

We successfully demonstrated the incorporation of dopant promoter metals (Nb, Zr, Ta, Hf) into the framework of Mo_2/KIT-6 catalysts by using a simple wet impregnation technique. The $Mo_2/Nb_{1.5}$-KIT-6 catalyst displayed enhanced and relatively stable propylene formation rate (54.2 ± 0.5 mmol $(mol_{Mo}\ s)^{-1}$) when compared to monometallic Mo_2/KIT-6 (28.7 ± 1.1 mmol $(mol_{Mo}\ s)^{-1}$) catalysts under identical reaction conditions. The addition of Nb is hypothesized to not only enhance the Mo dispersion but also create additional bimetallic active sites [$(O=)_2$Mo(-O-Nb)(-O-

Si)]. DR UV-Vis, Raman, and XAS analysis results collectively reveal that isolated monomeric di-oxo Mo^{VI} species (O=Mo=O) are the majority species followed by the presence of either oligomeric or polymerized MoO_x species in minor quantities. Raman analysis revealed that isolated Mo-dioxo precatalytic species exist on the fresh monometallic and bimetallic Mo-based formulations. The coordinatively unsaturated monomeric Mo^{VI} di-oxo species have been reported to be the precatalytic active sites for carbene formation in metathesis and exhibit Lewis acidity as inferred from *in situ* Py-FTIR experiments. Interestingly, pyridine adsorption energies on the Lewis acid metal centers on the monometallic and bimetallic catalysts are different. The correlation between the propylene formation rates and the adsorption enthalpies of pyridine reveals that Lewis acid metal centers with stronger electrophilic character likely aid in greater stabilization of the adsorbed olefins (by varying the O=M=O bond angle) yielding higher rates and selectivity for olefin metathesis. The study also highlights the significance of the ^{15}N average chemical shifts (δ_{avg}) of the metal substituted Py-M that are sensitive to site structure and allows us to discern different types of surface MoO_x species with differing electronic and coordination environments. The selective enhancement of metathesis activity of Mo-based catalysts upon the addition of a second metal such as Nb, Ta, or Zr is a significant result. It opens up a relatively simple technique for creating more active precatalytic sites and tuning catalyst activity, most likely by varying the O=M=O bond angle with the added metal. The insights and correlations developed by this technique provide an opportunity to explore the NMR signatures for transition metals and their relationships to electronic structure and reactivity. They also help facilitate catalyst design to optimize metal reactant binding energy to guide the redesign of active and durable bimetallic catalysts in general.

Associated Content

Supporting Information

Experimental procedure for catalysts characterization techniques, metathesis activity evaluation; comparative metathesis catalytic data; spent and regenerated catalytic data, and additional characterization data such as XRD, HAADF-STEM, XANES, EXAFS, DR UV-Vis, XPS, *in situ* FTIR spectroscopy, FTIR-Pyridine, TPD-NH_3, and ^{1}H, ^{13}C, and ^{15}N solid-state NMR.

Notes

The authors declare no competing financial interest.

Acknowledgements

The authors acknowledge financial support from the National Science Foundation (NSF-OIA - 1539105, NSF-NRT - 1922649), Center for Environmentally Beneficial Catalysis, University of Kansas Department of Chemical & Petroleum Engineering Summer Scholarship, Kansas Board of Regents, and Dan F. Servey Distinguished Professorship funds (BS). The authors also acknowledge the Canadian Light Source (CLS) at the University of Saskatchewan for providing the beamtime at BioXAS. Support for the NMR instrumentation was provided by NSF Chemical Instrumentation Grant # 0840515. The authors thank Dr. Prem Singh Thapa (Microscopy and Analytical Imaging Laboratory) at the University of Kansas for XPS analysis; Drs. Luan Nguyen and Yuting Li for technical assistance on EXAFS analysis; Dr. Robert Keyse of the Institute for Functional Materials and Devices at the Lehigh University for performing TEM characterization; Dr. Juan J. Bravo Suarez at the Center for Environmentally Beneficial Catalysis at the University of Kansas for providing us with the facility to perform Raman analysis. A part of this research (^{15}N solid-state NMR experiments at low temperature) was supported by the U.S. Department of Energy (DOE), Office of Science, Basic Energy Sciences, Chemical Sciences, Geosciences, and Biosciences Division, and was performed at the Ames National Laboratory, which is operated for the U.S. DOE by Iowa State University under contract # DE-AC02-07CH11358. The authors acknowledge Lukas Lätsch for helpful discussions on solid-state NMR.

Present Address

Anand Ramanathan: *Chevron Phillips Chemical Co LLC. Phillips 66 Research Center, Bartlesville, OK 74003. United States.*

REFERENCES

(1) Chen, S.; Chang, X.; Sun, G.; Zhang, T.; Xu, Y.; Wang, Y.; Pei, C.; Gong, J. Propane dehydrogenation: catalyst development, new chemistry, and emerging technologies. *Chemical Society Reviews* **2021**, *50* (5), 3315-3354. DOI: http://dx.doi.org/10.1039/D0CS00814A.

(2) National Academies of Sciences, E., and Medicine 2016. *The Changing Landscape of Hydrocarbon Feedstocks for Chemical Production: Implications for Catalysis: Proceedings of a Workshop. Washington, DC*.

(3) Shi, L.; Wang, Y.; Yan, B.; Song, W.; Shao, D.; Lu, A.-H. Progress in selective oxidative dehydrogenation of light alkanes to olefins promoted by boron nitride catalysts. *Chemical Communications* **2018**. DOI: https://doi.org/10.1039/C8CC04604B.

(4) Monai, M.; Gambino, M.; Wannakao, S.; Weckhuysen, B. M. Propane to olefins tandem catalysis: a selective route towards light olefins production. *Chemical Society Reviews* **2021**, 10.1039/D1CS00357G. DOI: https://doi.org/10.1039/D1CS00357G.

(5) National Academies of Sciences, E., and Medicine 2022. *New Directions for Chemical Engineering. Washington, DC:*; The National Academies Press. DOI: https://doi.org/10.17226/26342.

(6) Mol, J. C. Industrial applications of olefin metathesis. *Journal of Molecular Catalysis A: Chemical* **2004**, *213* (1), 39-45. DOI: https://doi.org/10.1016/j.molcata.2003.10.049.

(7) Mol, J. C. Industrial Applications of Olefin Metathesis. Dordrecht, 2003; Springer Netherlands: pp 313-322.

(8) Lwin, S.; Wachs, I. E. Olefin Metathesis by Supported Metal Oxide Catalysts. *ACS Catalysis* **2014**, *4* (8), 2505-2520. DOI: https://doi.org/10.1021/cs500528h.

(9) Debecker, D. P.; Schimmoeller, B.; Stoyanova, M.; Poleunis, C.; Bertrand, P.; Rodemerck, U.; Gaigneaux, E. M. Flame-made $MoO_3/SiO_2–Al_2O_3$ metathesis catalysts with highly dispersed and highly active molybdate species. *Journal of Catalysis* **2011**, *277* (2), 154-163. DOI: https://doi.org/10.1016/j.jcat.2010.11.003.

(10) Debecker, D. P.; Stoyanova, M.; Colbeau-Justin, F.; Rodemerck, U.; Boissière, C.; Gaigneaux, E. M.; Sanchez, C. One-Pot Aerosol Route to MoO_3-SiO_2-Al2O_3 Catalysts with Ordered Super Microporosity and High Olefin Metathesis Activity. *Angewandte Chemie International Edition* **2012**, *51* (9), 2129-2131. DOI: https://doi.org/10.1002/anie.201106277.

(11) Amakawa, K.; Wrabetz, S.; Kröhnert, J.; Tzolova-Müller, G.; Schlögl, R.; Trunschke, A. In Situ Generation of Active Sites in Olefin Metathesis. *Journal of the American Chemical Society* **2012**, *134* (28), 11462-11473. DOI: https://doi.org/10.1021/ja3011989.

(12) Hahn, T.; Bentrup, U.; Armbrüster, M.; Kondratenko, E. V.; Linke, D. The Enhancing Effect of Brønsted Acidity of Supported MoO_x Species on their Activity and Selectivity in Ethylene/trans-2-Butene Metathesis. *ChemCatChem* **2014**, *6* (6), 1664-1672. DOI: https://doi.org/10.1002/cctc.201400040.

(13) Ding, K.; Gulec, A.; Johnson, A. M.; Drake, T. L.; Wu, W.; Lin, Y.; Weitz, E.; Marks, L. D.; Stair, P. C. Highly Efficient Activation, Regeneration, and Active Site Identification of Oxide-Based Olefin Metathesis Catalysts. *ACS Catalysis* **2016**, *6* (9), 5740-5746. DOI: https://doi.org/10.1021/acscatal.6b00098.

(14) Ramanathan, A.; Wu, J.-F.; Maheswari, R.; Hu, Y.; Subramaniam, B. Synthesis of molybdenum-incorporated mesoporous silicates by evaporation-induced self-assembly: Insights into surface oxide species and corresponding olefin metathesis activity. *Microporous and*

Mesoporous Materials **2017**, *245*, 118-125. DOI: https://doi.org/10.1016/j.micromeso.2017.03.001.
(15) Uchagawkar, A.; Ramanathan, A.; Hu, Y.; Subramaniam, B. Highly dispersed molybdenum containing mesoporous silicate (Mo-TUD-1) for olefin metathesis. *Catalysis Today* **2020**, *343*, 215-225. DOI: https://doi.org/10.1016/j.cattod.2019.03.073.
(16) Skoda, D.; Zhu, R.; Hanulikova, B.; Styskalik, A.; Vykoukal, V.; Machac, P.; Simonikova, L.; Kuritka, I.; Poleunis, C.; Debecker, D. P.; Román-Leshkov, Y. Propylene Metathesis over Molybdenum Silicate Microspheres with Dispersed Active Sites. *ACS Catalysis* **2023**, *13* (19), 12970-12982. DOI: https://doi.org/10.1021/acscatal.3c02045.
(17) Debecker, D. P.; Bouchmella, K.; Poleunis, C.; Eloy, P.; Bertrand, P.; Gaigneaux, E. M.; Mutin, P. H. Design of SiO_2-Al_2O_3-MoO_3 Metathesis Catalysts by Nonhydrolytic Sol−Gel. *Chemistry of Materials* **2009**, *21* (13), 2817-2824. DOI: https://doi.org/10.1021/cm900490t.
(18) Chakrabarti, A.; Wachs, I. E. Activation Mechanism and Surface Intermediates during Olefin Metathesis by Supported MoO_x/Al_2O_3 Catalysts. *The Journal of Physical Chemistry C* **2019**, *123* (19), 12367-12375. DOI: https://doi.org/10.1021/acs.jpcc.9b02426.
(19) Vikulov, K. A.; Shelimov, B. N.; Kazansky, V. B.; Mol, J. C. Deactivation mechanism of photoreduced and cyclopropane-treated molybdena/silica catalysts for olefin metathesis. *Journal of Molecular Catalysis* **1994**, *90* (1), 61-67. DOI: https://doi.org/10.1016/0304-5102(93)E0304-Y.
(20) Mougel, V.; Chan, K.-W.; Siddiqi, G.; Kawakita, K.; Nagae, H.; Tsurugi, H.; Mashima, K.; Safonova, O.; Copéret, C. Low Temperature Activation of Supported Metathesis Catalysts by Organosilicon Reducing Agents. *ACS Central Science* **2016**, *2* (8), 569-576. DOI: https://doi.org/10.1021/acscentsci.6b00176.
(21) Roman, Y.; Zhang, S.; Consoli, D.; Shaikh, S. Promoters for Heterogeneous Olefin Metathesis. US 2020/0354291 A1 2020.
(22) Gani, T. Z. H.; Berkson, Z. J.; Zhu, R.; Kang, J. H.; Di Iorio, J. R.; Chan, K. W.; Consoli, D. F.; Shaikh, S. K.; Copéret, C.; Román-Leshkov, Y. Promoting active site renewal in heterogeneous olefin metathesis catalysts. *Nature* **2023**, *617* (7961), 524-528. DOI: https://doi.org/10.1038/s41586-023-05897-w.
(23) Gayapan, K.; Sripinun, S.; Panpranot, J.; Praserthdam, P.; Assabumrungrat, S. Effects of calcination and pretreatment temperatures on the catalytic activity and stability of H_2-treated WO_3/SiO_2 catalysts in metathesis of ethylene and 2-butene. *RSC Advances* **2018**, *8* (50), 28555-28568. DOI: https://doi.org/10.1039/C8RA04949A.
(24) Michorczyk, P.; Węgrzyniak, A.; Węgrzynowicz, A.; Handzlik, J. Simple and Efficient Way of Molybdenum Oxide-Based Catalyst Activation for Olefins Metathesis by Methane Pretreatment. *ACS Catalysis* **2019**, *9* (12), 11461-11467. DOI: https://doi.org/10.1021/acscatal.9b03714.
(25) Zhu, H.; Ramanathan, A.; Wu, J.-F.; Subramaniam, B. Genesis of Strong Brønsted Acid Sites in WZr-KIT-6 Catalysts and Enhancement of Ethanol Dehydration Activity. *ACS Catalysis* **2018**, *8* (6), 4848-4859. DOI: https://doi.org/10.1021/acscatal.8b00480.
(26) Maheswari, R.; Ramanathan, A.; Zhu, H.; Araújo do Nascimento Araújo, A.; Chapman, C.; Tang, Y.; Tao, F.; Subramaniam, B. Enhanced Friedel-Crafts benzylation activity of bimetallic WSn-KIT-6 catalysts. *Journal of Catalysis* **2020**, *389*, 657-666. DOI: https://doi.org/10.1016/j.jcat.2020.07.001.

(27) Lan, X.; Wang, T. Highly Selective Catalysts for the Hydrogenation of Unsaturated Aldehydes: A Review. *ACS Catalysis* **2020**, *10* (4), 2764-2790. DOI: https://doi.org/10.1021/acscatal.9b04331.
(28) Wu, J.-F.; Ramanathan, A.; Kersting, R.; Jystad, A. M.; Zhu, H.; Hu, Y.; Marshall, C. P.; Caricato, M.; Subramaniam, B. Enhanced Olefin Metathesis Performance of Tungsten and Niobium Incorporated Bimetallic Silicates: Evidence of Synergistic Effects. *ChemCatChem* **2020**, *12*, 2004–2013. DOI: https://doi.org/10.1002/cctc.201902131.
(29) Zhang, B.; Xiang, S.; Frenkel, A. I.; Wachs, I. E. Molecular Design of Supported MoO_x Catalysts with Surface TaO_x Promotion for Olefin Metathesis. *ACS Catalysis* **2022**, 3226-3237. DOI: https://doi.org/10.1021/acscatal.1c06000.
(30) Otroshchenko, T.; Zhang, Q.; Kondratenko, E. V. Enhancing Propene Formation in the Metathesis of Ethylene with 2-Butene at Close to Room Temperature over MoO_x/SiO_2 through Support Promotion with P, Cl, or S. *ACS Catalysis* **2021**, 14159-14167. DOI: https://doi.org/10.1021/acscatal.1c04267.
(31) Otroshchenko, T.; Zhang, Q.; Kondratenko, E. V. Room-Temperature Metathesis of Ethylene with 2-Butene to Propene Over MoO_x-Based Catalysts: Mixed Oxides as Perspective Support Materials. *Catalysis Letters* **2021**. DOI: https://doi.org/10.1007/s10562-021-03822-2.
(32) Ramanathan, A.; Subramaniam, B. Metal-Incorporated Mesoporous Silicates: Tunable Catalytic Properties and Applications. *Molecules* **2018**, *23* (2), 263. DOI: https://doi.org/10.3390/molecules23020263.
(33) Afanasiev, P. Structure and Properties of the $Mo_3Nb_2O_{14}$ Oxide. *The Journal of Physical Chemistry B* **2005**, *109* (39), 18293-18300. DOI: https://doi.org/10.1021/jp050554u.
(34) Otroshchenko, T.; Reinsdorf, O.; Linke, D.; Kondratenko, E. V. A chemical titration method for quantification of carbenes in Mo- or W-containing catalysts for metathesis of ethylene with 2-butenes: verification and application potential. *Catalysis Science & Technology* **2019**, *9* (20), 5660-5667. DOI: https://doi.org/10.1039/C9CY01697J.
(35) Berkson, Z. J.; Bernhardt, M.; Schlapansky, S. L.; Benedikter, M. J.; Buchmeiser, M. R.; Price, G. A.; Sunley, G. J.; Copéret, C. Olefin-Surface Interactions: A Key Activity Parameter in Silica-Supported Olefin Metathesis Catalysts. *JACS Au* **2022**, *2* (3), 777-786. DOI: https://doi.org/10.1021/jacsau.2c00052.
(36) Jeziorowski, H.; Knoezinger, H. Raman and ultraviolet spectroscopic characterization of molybdena on alumina catalysts. *The Journal of Physical Chemistry* **1979**, *83* (9), 1166-1173. DOI: https://doi.org/10.1021/j100472a012.
(37) Williams, C. C.; Ekerdt, J. G.; Jehng, J. M.; Hardcastle, F. D.; Turek, A. M.; Wachs, I. E. A Raman and ultraviolet diffuse reflectance spectroscopic investigation of silica-supported molybdenum oxide. *The Journal of Physical Chemistry* **1991**, *95* (22), 8781-8791. DOI: https://doi.org/10.1021/j100175a067.
(38) Jarupatrakorn, J.; Coles, M. P.; Tilley, T. D. Synthesis and Characterization of $MO[OSi(OtBu)_3]_4$ and $MO_2[OSi(OtBu)_3]_2$ (M = Mo, W): Models for Isolated Oxo-Molybdenum and -Tungsten Sites on Silica and Precursors to Molybdena− and Tungsta−Silica Materials. *Chemistry of Materials* **2005**, *17* (7), 1818-1828. DOI: https://doi.org/10.1021/cm040344e.
(39) Fournier, M.; Louis, C.; Che, M.; Chaquin, P.; Masure, D. Polyoxometallates as models for oxide catalysts: Part I. An UV-visible reflectance study of polyoxomolybdates: Influence of polyhedra arrangement on the electronic transitions and comparison with supported molybdenum catalysts. *Journal of Catalysis* **1989**, *119* (2), 400-414. DOI: https://doi.org/10.1016/0021-9517(89)90170-X.

(40) Bulánek, R.; Čapek, L.; Setnička, M.; Čičmanec, P. DR UV–vis Study of the Supported Vanadium Oxide Catalysts. *The Journal of Physical Chemistry C* **2011**, *115* (25), 12430-12438. DOI: https://10.1021/jp112206c.
(41) Ebrahimipour, S. Y.; Khabazadeh, H.; Castro, J.; Sheikhshoaie, I.; Crochet, A.; Fromm, K. M. cis-Dioxido-molybdenum(VI) complexes of tridentate ONO hydrazone Schiff base: Synthesis, characterization, X-ray crystal structure, DFT calculation and catalytic activity. *Inorganica Chimica Acta* **2015**, *427*, 52-61. DOI: https://doi.org/10.1016/j.ica.2014.11.023.
(42) Seghir, I.; Nadia, N.; Meftah, Y.; Hachani, S.; Samira, M. DFT/TDDFT Investigation on the Electronic Structure and Spectroscopic Properties of Cis-Dioxomolybdenum (VI) Complexes. *Acta Chimica Slovenica* **2019**, *66*. DOI: https://10.17344/acsi.2019.5044.
(43) Capel-Sanchez, M. C.; dela Peña-O'Shea, V. A.; Barrio, L.; Campos-Martin, J. M.; Fierro, J. L. G. TD-DFT analysis of the electronic spectra of Ti-containing catalysts. *Topics in Catalysis* **2006**, *41* (1), 27-34. DOI: https://10.1007/s11244-006-0091-9.
(44) Thielemann, J. P.; Ressler, T.; Walter, A.; Tzolova-Müller, G.; Hess, C. Structure of molybdenum oxide supported on silica SBA-15 studied by Raman, UV–Vis and X-ray absorption spectroscopy. *Applied Catalysis A: General* **2011**, *399* (1), 28-34. DOI: https://doi.org/10.1016/j.apcata.2011.03.032.
(45) Masure, D.; Chaquin, P.; Louis, C.; Che, M.; Fournier, M. Polyoxometallates as models for oxide catalysts: Part II. Theoretical semi-empirical approach to the influence of the inner and outer Mo coordination spheres on the electronic levels of polyoxomolybdates. *Journal of Catalysis* **1989**, *119* (2), 415-425. DOI: https://doi.org/10.1016/0021-9517(89)90171-1.
(46) Weber, R. S. Effect of Local Structure on the UV-Visible Absorption Edges of Molybdenum Oxide Clusters and Supported Molybdenum Oxides. *Journal of Catalysis* **1995**, *151* (2), 470-474. DOI: https://doi.org/10.1006/jcat.1995.1052.
(47) Lee, E. L.; Wachs, I. E. In Situ Spectroscopic Investigation of the Molecular and Electronic Structures of SiO2 Supported Surface Metal Oxides. *The Journal of Physical Chemistry C* **2007**, *111* (39), 14410-14425. DOI: https://doi.org/10.1021/jp0735482.
(48) Lee, E. L.; Wachs, I. E. Molecular Design and In Situ Spectroscopic Investigation of Multilayered Supported $M_1O_x/M_2O_x/SiO_2$ Catalysts. *The Journal of Physical Chemistry C* **2008**, *112* (51), 20418-20428. DOI: https://doi.org/10.1021/jp805265m.
(49) Tian, H.; Roberts, C. A.; Wachs, I. E. Molecular Structural Determination of Molybdena in Different Environments: Aqueous Solutions, Bulk Mixed Oxides, and Supported MoO_3 Catalysts. *The Journal of Physical Chemistry C* **2010**, *114* (33), 14110-14120. DOI: https://doi.org/10.1021/jp103269w.
(50) Bare, S. R.; Mitchell, G. E.; Maj, J. J.; Vrieland, G. E.; Gland, J. L. Local site symmetry of dispersed molybdenum oxide catalysts: XANES at the Mo $L_{2,3}$-edges. *The Journal of Physical Chemistry* **1993**, *97* (22), 6048-6053. DOI: https://doi.org/10.1021/j100124a043.
(51) Yamamoto, T. Assignment of pre-edge peaks in K-edge x-ray absorption spectra of 3d transition metal compounds: electric dipole or quadrupole? *X-Ray Spectrometry* **2008**, *37* (6), 572-584. DOI: https://doi.org/10.1002/xrs.1103.
(52) Hu, H.; Wachs, I. E.; Bare, S. R. Surface Structures of Supported Molybdenum Oxide Catalysts: Characterization by Raman and Mo L_3-Edge XANES. *The Journal of Physical Chemistry* **1995**, *99* (27), 10897-10910. DOI: https://doi.org/10.1021/j100027a034.
(53) Radhakrishnan, R.; Reed, C.; Oyama, S. T.; Seman, M.; Kondo, J. N.; Domen, K.; Ohminami, Y.; Asakura, K. Variability in the Structure of Supported MoO_3 Catalysts: Studies Using Raman

and X-ray Absorption Spectroscopy with ab Initio Calculations. *The Journal of Physical Chemistry B* **2001**, *105* (36), 8519-8530. DOI: https://doi.org/10.1021/jp0117361.
(54) Xie, S.; Chen, K.; Bell, A. T.; Iglesia, E. Structural Characterization of Molybdenum Oxide Supported on Zirconia. *The Journal of Physical Chemistry B* **2000**, *104* (43), 10059-10068. DOI: https://doi.org/10.1021/jp002419h.
(55) Tsilomelekis, G.; Boghosian, S. On the configuration, molecular structure and vibrational properties of MoO_x sites on alumina, zirconia, titania and silica. *Catalysis Science & Technology* **2013**, *3* (8), 1869-1888, 10.1039/C3CY00057E. DOI: https://doi.org/10.1039/C3CY00057E.
(56) Kurleto, K.; Tielens, F.; Handzlik, J. Isolated Molybdenum(VI) and Tungsten(VI) Oxide Species on Partly Dehydroxylated Silica: A Computational Perspective. *The Journal of Physical Chemistry C* **2020**, *124* (5), 3002-3013. DOI: https://doi.org/10.1021/acs.jpcc.9b09586.
(57) Chempath, S.; Zhang, Y.; Bell, A. T. DFT Studies of the Structure and Vibrational Spectra of Isolated Molybdena Species Supported on Silica. *The Journal of Physical Chemistry C* **2007**, *111* (3), 1291-1298. DOI: https://doi.org/10.1021/jp064741j.
(58) Zhang, B.; Ford, M. E.; Ream, E.; Wachs, I. E. Olefin metathesis over supported MoOx catalysts: influence of the oxide support. *Catalysis Science & Technology* **2023**. DOI: https://10.1039/D2CY01612E.
(59) Handzlik, J.; Ogonowski, J. Structure of Isolated Molybdenum(VI) and Molybdenum(IV) Oxide Species on Silica: Periodic and Cluster DFT Studies. *The Journal of Physical Chemistry C* **2012**, *116* (9), 5571-5584. DOI: https://doi.org/10.1021/jp207385h.
(60) Vuurman, M. A.; Wachs, I. E. In situ Raman spectroscopy of alumina-supported metal oxide catalysts. *The Journal of Physical Chemistry* **1992**, *96* (12), 5008-5016. DOI: https://doi.org/10.1021/j100191a051.
(61) Handzlik, J.; Sautet, P. Structure of Isolated Molybdenum(VI) Oxide Species on γ-Alumina: A Periodic Density Functional Theory Study. *The Journal of Physical Chemistry C* **2008**, *112* (37), 14456-14463. DOI: https://doi.org/10.1021/jp802372e.
(62) Berkson, Z. J.; Zhu, R.; Ehinger, C.; Lätsch, L.; Schmid, S. P.; Nater, D.; Pollitt, S.; Safonova, O. V.; Björgvinsdóttir, S.; Barnes, A. B.; Román-Leshkov, Y.; Price, G. A.; Sunley, G. J.; Copéret, C. Active Site Descriptors from ^{95}Mo NMR Signatures of Silica-Supported Mo-Based Olefin Metathesis Catalysts. *Journal of the American Chemical Society* **2023**, *145* (23), 12651-12662. DOI: https://doi.org/10.1021/jacs.3c02201.
(63) Amakawa, K.; Kröhnert, J.; Wrabetz, S.; Frank, B.; Hemmann, F.; Jäger, C.; Schlögl, R.; Trunschke, A. Active Sites in Olefin Metathesis over Supported Molybdena Catalysts. *ChemCatChem* **2015**, *7* (24), 4059-4065. DOI: https://10.1002/cctc.201500725.
(64) Handzlik, J.; Kurleto, K.; Gierada, M. Computational Insights into Active Site Formation during Alkene Metathesis over a MoO_x/SiO_2 Catalyst: The Role of Surface Silanols. *ACS Catalysis* **2021**, *11* (21), 13575-13590. DOI: https://10.1021/acscatal.1c03912.
(65) Dulaurent, O.; Nawdali, M.; Bourane, A.; Bianchi, D. Heat of adsorption of carbon monoxide on a Ru/Al_2O_3 catalyst using adsorption equilibrium conditions at high temperatures. *Applied Catalysis A: General* **2000**, *201* (2), 271-279. DOI: https://doi.org/10.1016/S0926-860X(00)00447-6.
(66) Bourane, A.; Dulaurent, O.; Chandes, K.; Bianchi, D. Heats of adsorption of the linear CO species on a Pt/Al_2O_3 catalyst using FTIR spectroscopy: Comparison between TPD and adsorption equilibrium procedures. *Applied Catalysis A: General* **2001**, *214* (2), 193-202. DOI: https://doi.org/10.1016/S0926-860X(01)00483-5.

(67) Bregante, D. T.; Thornburg, N. E.; Notestein, J. M.; Flaherty, D. W. Consequences of Confinement for Alkene Epoxidation with Hydrogen Peroxide on Highly Dispersed Group 4 and 5 Metal Oxide Catalysts. *ACS Catalysis* **2018**, *8* (4), 2995-3010. DOI: https://doi.org/10.1021/acscatal.7b03986.
(68) Gurinov, A. A.; Rozhkova, Y. A.; Zukal, A.; Čejka, J.; Shenderovich, I. G. Mutable Lewis and Brønsted Acidity of Aluminated SBA-15 as Revealed by NMR of Adsorbed Pyridine-^{15}N. *Langmuir* **2011**, *27* (19), 12115-12123. DOI: https://doi.org/10.1021/la2017566.
(69) Zhang, W.; Xu, S.; Han, X.; Bao, X. In situ solid-state NMR for heterogeneous catalysis: a joint experimental and theoretical approach. *Chemical Society Reviews* **2012**, *41* (1), 192-210, 10.1039/C1CS15009J. DOI: https://doi.org/10.1039/C1CS15009J.
(70) Hunger, M. Brønsted Acid Sites in Zeolites Characterized by Multinuclear Solid-State NMR Spectroscopy. *Catalysis Reviews* **1997**, *39* (4), 345-393. DOI: https://doi.org/10.1080/01614949708007100.
(71) Xu, J.; Zheng, A.; Yang, J.; Su, Y.; Wang, J.; Zeng, D.; Zhang, M.; Ye, C.; Deng, F. Acidity of Mesoporous MoO_x/ZrO_2 and WO_x/ZrO_2 Materials: A Combined Solid-State NMR and Theoretical Calculation Study. *The Journal of Physical Chemistry B* **2006**, *110* (22), 10662-10671. DOI: https://doi.org/10.1021/jp0614087.
(72) Shenderovich, I. G.; Buntkowsky, G.; Schreiber, A.; Gedat, E.; Sharif, S.; Albrecht, J.; Golubev, N. S.; Findenegg, G. H.; Limbach, H.-H. Pyridine-^{15}N A Mobile NMR Sensor for Surface Acidity and Surface Defects of Mesoporous Silica. *The Journal of Physical Chemistry B* **2003**, *107* (43), 11924-11939. DOI: https://doi.org/10.1021/jp0349740.
(73) Pretsch, E.; Bühlmann, P.; Badertscher, M. *Structure determination of organic compounds*; Springer-Verlag: Berlin Heidelberg, 2009.
(74) Hu, J. Z.; Kwak, J. H.; Wang, Y.; Hu, M. Y.; Turcu, R. V.; Peden, C. H. F. Characterizing Surface Acidic Sites in Mesoporous-Silica-Supported Tungsten Oxide Catalysts Using Solid-State NMR and Quantum Chemistry Calculations. *The Journal of Physical Chemistry C* **2011**, *115* (47), 23354-23362. DOI: https://doi.org/10.1021/jp203813f.
(75) Moroz, I. B.; Larmier, K.; Liao, W.-C.; Copéret, C. Discerning γ-Alumina Surface Sites with Nitrogen-15 Dynamic Nuclear Polarization Surface Enhanced NMR Spectroscopy of Adsorbed Pyridine. *The Journal of Physical Chemistry C* **2018**, *122* (20), 10871-10882. DOI: https://doi.org/10.1021/acs.jpcc.8b01823.
(76) Gunther, W. R.; Michaelis, V. K.; Griffin, R. G.; Román-Leshkov, Y. Interrogating the Lewis Acidity of Metal Sites in Beta Zeolites with ^{15}N Pyridine Adsorption Coupled with MAS NMR Spectroscopy. *The Journal of Physical Chemistry C* **2016**, *120* (50), 28533-28544. DOI: https://doi.org/10.1021/acs.jpcc.6b07811.
(77) Shimizu, K.; Venkatraman, T. N.; Song, W. NMR study of tungstated zirconia catalyst: acidic properties of tungstated zirconia and influence of tungsten loading. *Applied Catalysis A: General* **2002**, *224* (1), 77-87. DOI: https://doi.org/10.1016/S0926-860X(01)00737-2.
(78) Dijkstra, T. W.; Duchateau, R.; van Santen, R. A.; Meetsma, A.; Yap, G. P. A. Silsesquioxane Models for Geminal Silica Surface Silanol Sites. A Spectroscopic Investigation of Different Types of Silanols. *Journal of the American Chemical Society* **2002**, *124* (33), 9856-9864. DOI: https://doi.org/10.1021/ja0122243.
(79) Moroz, I. B.; Lund, A.; Kaushik, M.; Severy, L.; Gajan, D.; Fedorov, A.; Lesage, A.; Copéret, C. Specific Localization of Aluminum Sites Favors Ethene-to-Propene Conversion on (Al)MCM-41-Supported Ni(II) Single Sites. *ACS Catalysis* **2019**, *9* (8), 7476-7485. DOI: https://10.1021/acscatal.9b01903.

(80) Jystad, A.; Leblanc, H.; Caricato, M. Surface Acidity Characterization of Metal-Doped Amorphous Silicates via Py-FTIR and ^{15}N NMR Simulations. *The Journal of Physical Chemistry C* **2020**, *124* (28), 15231-15240. DOI: https://doi.org/10.1021/acs.jpcc.0c03292.
(81) Haw, J. F.; Zhang, J.; Shimizu, K.; Venkatraman, T. N.; Luigi, D.-P.; Song, W.; Barich, D. H.; Nicholas, J. B. NMR and Theoretical Study of Acidity Probes on Sulfated Zirconia Catalysts. *Journal of the American Chemical Society* **2000**, *122* (50), 12561-12570. DOI: https://doi.org/10.1021/ja0027721.
(82) Henker, M.; Wendlandt, K.-P.; Valyon, J.; Bornmann, P. Structure of MoO_3/Al_2O_3-SiO_2 catalysts. *Applied Catalysis* **1991**, *69* (1), 205-220. DOI: https://doi.org/10.1016/S0166-9834(00)83303-5.
(83) Rajagopal, S.; Marzari, J. A.; Miranda, R. Silica-Alumina-Supported Mo Oxide Catalysts: Genesis and Demise of Brønsted-Lewis Acidity. *Journal of Catalysis* **1995**, *151* (1), 192-203. DOI: https://doi.org/10.1006/jcat.1995.1021.
(84) Ramírez, J.; Gutiérrez-Alejandre, A. Characterization and Hydrodesulfurization Activity of W-Based Catalysts Supported on Al_2O_3–TiO_2 Mixed Oxides. *Journal of Catalysis* **1997**, *170* (1), 108-122. DOI: https://doi.org/10.1006/jcat.1997.1713.
(85) Reddy, B. M.; Chowdhury, B.; Smirniotis, P. G. An XPS study of the dispersion of MoO3 on TiO_2–ZrO_2, TiO_2–SiO_2, TiO_2–Al_2O_3, SiO_2–ZrO_2, and SiO_2–TiO_2–ZrO_2 mixed oxides. *Applied Catalysis A: General* **2001**, *211* (1), 19-30. DOI: https://doi.org/10.1016/S0926-860X(00)00834-6.
(86) Copéret, C.; Liao, W.-C.; Gordon, C. P.; Ong, T.-C. Active Sites in Supported Single-Site Catalysts: An NMR Perspective. *Journal of the American Chemical Society* **2017**, *139* (31), 10588-10596. DOI: https://doi.org/10.1021/jacs.6b12981.
(87) Amakawa, K.; Sun, L.; Guo, C.; Hävecker, M.; Kube, P.; Wachs, I. E.; Lwin, S.; Frenkel, A. I.; Patlolla, A.; Hermann, K.; Schlögl; Trunschke, A. How Strain Affects the Reactivity of Surface Metal Oxide Catalysts. *Angewandte Chemie International Edition* **2013**, *52* (51), 13553-13557. DOI: https://doi.org/10.1002/anie.201306620.
(88) Berkson, Z. J.; Lätsch, L.; Hillenbrand, J.; Fürstner, A.; Copéret, C. Classifying and Understanding the Reactivities of Mo-Based Alkyne Metathesis Catalysts from ^{95}Mo NMR Chemical Shift Descriptors. *Journal of the American Chemical Society* **2022**, *144* (33), 15020-15025. DOI: https://doi.org/10.1021/jacs.2c06252.

Table of Contents (TOC) graphic